

ARMY RESEARCH LABORATORY



Coilable Crystalline Fiber (CCF) Lasers and their Scalability

by Mark Dubinskiy, Larry D. Merkle, and Helmuth Meissner

ARL-TR-6850

March 2014

NOTICES

Disclaimers

The findings in this report are not to be construed as an official Department of the Army position unless so designated by other authorized documents.

Citation of manufacturer's or trade names does not constitute an official endorsement or approval of the use thereof.

Destroy this report when it is no longer needed. Do not return it to the originator.

Army Research Laboratory

Adelphi, MD 20783-1197

ARL-TR-6850

March 2014

Coilable Crystalline Fiber (CCF) Lasers and their Scalability

Mark Dubinskiy and Larry D. Merkle
Sensors and Electron Devices Directorate

Helmuth Meissner
Onyx Optics

REPORT DOCUMENTATION PAGE
*Form Approved
OMB No. 0704-0188*

Public reporting burden for this collection of information is estimated to average 1 hour per response, including the time for reviewing instructions, searching existing data sources, gathering and maintaining the data needed, and completing and reviewing the collection information. Send comments regarding this burden estimate or any other aspect of this collection of information, including suggestions for reducing the burden, to Department of Defense, Washington Headquarters Services, Directorate for Information Operations and Reports (0704-0188), 1215 Jefferson Davis Highway, Suite 1204, Arlington, VA 22202-4302. Respondents should be aware that notwithstanding any other provision of law, no person shall be subject to any penalty for failing to comply with a collection of information if it does not display a currently valid OMB control number.

PLEASE DO NOT RETURN YOUR FORM TO THE ABOVE ADDRESS.

1. REPORT DATE (DD-MM-YYYY) March 2014		2. REPORT TYPE		3. DATES COVERED (From - To)	
4. TITLE AND SUBTITLE Coilable Crystalline Fiber (CCF) Lasers and their Scalability				5a. CONTRACT NUMBER	
				5b. GRANT NUMBER	
				5c. PROGRAM ELEMENT NUMBER	
6. AUTHOR(S) Mark Dubinskiy, Larry D. Merkle, and Helmuth Meissner				5d. PROJECT NUMBER	
				5e. TASK NUMBER	
				5f. WORK UNIT NUMBER	
7. PERFORMING ORGANIZATION NAME(S) AND ADDRESS(ES) U.S. Army Research Laboratory ATTN: RDRL-SEE-M 2800 Powder Mill Road Adelphi, MD 20783-1197				8. PERFORMING ORGANIZATION REPORT NUMBER ARL-TR-6850	
9. SPONSORING/MONITORING AGENCY NAME(S) AND ADDRESS(ES)				10. SPONSOR/MONITOR'S ACRONYM(S)	
				11. SPONSOR/MONITOR'S REPORT NUMBER(S)	
12. DISTRIBUTION/AVAILABILITY STATEMENT Approved for public release; distribution unlimited.					
13. SUPPLEMENTARY NOTES					
14. ABSTRACT Conventional fiber lasers offer excellent beam quality and efficiency for high power lasers, but their composition (glass) poses significant disadvantages in pump absorption, gain, and thermal conductivity. All-crystalline fiber lasers, particularly if double-clad, would improve all these properties, greatly facilitating power scaling. Yet, progress in fabricating all-crystalline fibers has been limited thus far. The U.S. Army Research Laboratory (ARL) in partnership with Onyx Optics studied fully crystalline waveguides fabricated using current bonding techniques, with geometry similar to conventional double-clad fibers. We measured refractive indices to determine the parameters for erbium- or thulium-doped YAG ($Y_3Al_5O_{12}$)/YAG/spinel ($MgAl_2O_4$) double-clad waveguides with a single-mode core. We also investigated YAG doped with ytterbium as an inner cladding material, as its index can be adjusted to facilitate design of a single-mode core with large area. We characterized the thermal conductivity of nominally polycrystalline samples of each material. We performed laser experiments on both single- and double-clad Er:YAG cores of different sizes, and have obtained world's-first and world-record laser performance. This includes 25-W continuous wave (CW) output due to cladding-pumping of what we believe is the first truly double-clad all-crystalline YAG waveguide laser, and a record room-temperature slope efficiency (with respect to absorbed pump) of nearly 93 % with excellent beam quality from a core-pumped waveguide.					
15. SUBJECT TERMS laser, fiber, waveguide, single crystal, ceramic, double-clad, YAG, spinel, erbium, thulium, ytterbium					
16. SECURITY CLASSIFICATION OF:			17. LIMITATION OF ABSTRACT UU	18. NUMBER OF PAGES 58	19a. NAME OF RESPONSIBLE PERSON Larry D. Merkle
a. REPORT Unclassified	b. ABSTRACT Unclassified	c. THIS PAGE Unclassified			19b. TELEPHONE NUMBER (Include area code) 301-394-0941

Standard Form 298 (Rev. 8/98)

Prescribed by ANSI Std. Z39.18

Contents

List of Figures	v
List of Tables	vii
Acknowledgments	viii
Summary	1
1. Introduction	3
1.1 Rationale.....	3
1.2 Brief Review of Research Plan	5
1.3 Major Project Developments and Results	6
2. Development of the AFB-Based Bonded Doped/Undoped YAG Waveguiding Parts (Double-Clad Crystalline Fibers)	6
2.1 Refractive Index Measurement Samples.....	7
2.2 Refractive Index Results	7
3. Mode Simulation of Tm:YAG Double-Clad Waveguide Structures	10
3.1 Numerical Aperture (NA)	10
3.2 Single-Mode Condition	11
3.3 Mode Intensity Distribution	12
4. Thermal Conductivity of Ceramic Spinel (To Be Used As Outer Cladding)	14
4.1 Sample	14
4.2 Thermal Conductivity.....	14
4.3 Interface Heat Transfer Coefficient.....	16
4.4 Possible Thermal Issues with TA&T Spinel	17
4.4.1 X-Ray Diffraction Spectrum	17
4.4.2 NewView Microscope Images	20
4.4.3 Low Thermal Conductivity Spinel Samples	22
5. Laser Experiments	23

6. Closing Remarks on the Successful Year 1 Program	24
7. References	26
Appendix A. High Efficiency, Resonantly Diode Pumped, True Double-Clad, Er:YAG-Core, Waveguide Laser	29
Appendix B. Resonantly-Pumped Single-Mode Channel Waveguide Er:YAG Laser With Nearly Quantum Defect Limited Efficiency	39
List of Symbols, Abbreviations, and Acronyms	45
Distribution List	47

List of Figures

Figure 1. Contour plot of scalability of an Yb^{3+} -silica fiber vs. $\text{Yb}^{3+}:\text{YAG}$ fiber laser in the single frequency laser/amplifier case. Contour lines are output power in kW. In the yellow region, the laser output power is limited by stimulated Brillouin scattering; in the pink region, the limit is thermal lensing in the waveguide; in the blue region, the limit is pump diode brightness; and in the gray region, the output power is damage-limited (8).	4
Figure 2. Flexible YAG strip of $200 \times 10 \times 0.047 \text{ mm}^3$, bent over a 300-mm-diameter optic.	4
Figure 3. YAG strip of $50 \mu\text{m}$ thickness is predicted to have a minimum bending radius of $\sim 20 \text{ mm}$ before breakage. Red lines: The line at 450 MPa intersects the green curve to determine the maximum load; the resulting vertical line intersects the blue curve to determine the minimum radius of curvature, which can be read off by following the lower horizontal line.	5
Figure 4. Simplified design of Year-1 CCF.	6
Figure 5. Doublet designs for refractive index measurements. Dimensions are in mm.	7
Figure 6. Absorption coefficient at 1532 nm and refractive index changes at 1550 nm of Er-doped YAG vs. doping concentration. Neglecting the results measured from the 3%Er:YAG, the fitted refractive index change is $2.1 \times 10^{-4} \text{ /%}$; absorption coefficient is $2.8 \text{ cm}^{-1} \text{ /%}$	9
Figure 7. Absorption coefficient at 969 nm and refractive index changes at 1550 nm of Yb-doped YAG vs. doping concentration. Neglecting the absorption measured from the 10% Yb:YAG, the fitted refractive index changes is $1.6 \times 10^{-4} \text{ /%}$; absorption coefficient is $1.06 \text{ cm}^{-1} \text{ /%}$	9
Figure 8. Absorption coefficient at 786 nm and refractive index changes at 1550 nm of Tm-doped YAG vs. doping concentration. The fitted refractive index change is $2.08 \times 10^{-4} \text{ /%}$; absorption coefficient is $0.997 \text{ cm}^{-1} \text{ /%}$	10
Figure 9. Schematic illustration of double-clad Tm:YAG waveguide-fiber structure. The structure uses undoped YAG as inner cladding and spinel as outer cladding. The design is for laser diode cladding-pumped 2- μm crystalline waveguide Tm:YAG laser.	11
Figure 10. Theoretical single-mode waveguide core width as a function of Tm doping concentration.	11
Figure 11. Simulated two-dimensional (2-D) and three-dimensional (3-D) field distributions inside the 4%Tm:YAG square core waveguide with core width of $20 \mu\text{m}$	12
Figure 12. Field distributions along x- and y-axis (identical). Fundamental mode radius is $\sim 13.1 \mu\text{m}$ at $1/e^2$. Mode area is around $\sim 539 \mu\text{m}^2$	12
Figure 13. Simulated 2-D and 3-D field distributions inside 4%Tm:YAG square core waveguide with core width of $28 \mu\text{m}$	13
Figure 14. Field distributions along x- and y-axis (identical) of 2%Tm:YAG waveguide. Mode radius is $\sim 18.4 \mu\text{m}$ at $1/e^2$. Mode area $\sim 1060 \mu\text{m}^2$	13

Figure 15. Schematic illustration of AFB spinel-YAG composite used in the interferometric measurement.	14
Figure 16. OPD changes as a function of temperature for TA&T-manufactured ceramic spinel (C-spinel).	15
Figure 17. OPD changes as a function of temperature for undoped YAG.	15
Figure 18. Temperature as a function of distance inside the YAG and spinel portions of Sample #1.	16
Figure 19. Temperature as a function of distance inside the YAG and spinel portions of Sample #2.	16
Figure 20. Temperature distribution inside Sample #2. Left: full sample. Right: detail around the interface.	17
Figure 21. Schematic illustration of the TA&T spinel sample and the positions used for X-ray measurements (red dots). For each face, the three-integer symbols indicate candidate crystallographic directions that were considered, and the symbols in red denote the orientations that best fit the data. For the large face, the green symbol indicates the reassigned direction discussed in the text.	18
Figure 22. Typical x-ray spectra measured at several spots on the large spinel surfaces. The shaded region highlights the 5.31 keV region discussed in the text.	18
Figure 23. Typical x-ray spectra measured at several spots on the side spinel surfaces. The shaded region highlights the 5.31 keV region discussed in the text.	20
Figure 24. X-ray spectra (several scans) on the end spinel surface. The shaded region highlights the 9.1 keV region noted in the text.	20
Figure 25. NewView microscope image taken from the large, side and end surfaces of the TA&T high thermal conductivity spinel. (By contrast, see figure 27, which has clear evidence of grain structure.)	21
Figure 26. Refined proposed crystal orientation of TA&T spinel.	21
Figure 27. NewView image of the relative lower thermal conductive spinel sample. The image size are x=0.35 mm and y=0.27 mm.	22
Figure 28. X-ray spectra of the low thermal conductivity TA&T spinel sample, for multiple spots on three faces, similar to those used in figures 21–24.	23
Figure 29. X-ray spectra of MER spinel taken at several spots.	23
Figure A-1. (a) The end-face photograph of the double-clad, Er^{3+} :YAG-core, channel waveguide, as described in the paper body; core – single-crystalline Er^{3+} (1%):YAG, inner cladding – single-crystalline undoped YAG, outer cladding - transparent ceramic magnesium aluminum spinel (MgAl_2O_4) and (b) The rendering of the waveguide with overall dimensions.	31
Figure A-2. A simplified optical layout of the cladding-pumped Er^{3+} :YAG/YAG channel waveguide laser. The pumping source, a fiber coupled InGaAsP/InP laser diode module (FCLDM) at 1532 nm, is described in the paper body. M1 and M2 are the cavity mirrors. L1 and L2 are the lenses of pump coupling optics.	31
Figure A-3. The absorption cross-section of the $^4I_{15/2} \rightarrow ^4I_{13/2}$ transitions of Er^{3+} in YAG at 300 K (blue, solid line). Spectrum of the laser diode module (purple, dashed line).	32

Figure A-4. The output power of the Er(1%):YAG/YAG channel waveguide laser at 1645 nm versus the incident pump power. Laser cavity: $L_{cav} = 35$ mm, flat HR mirror, output coupler with the reflectivity of $R_{OC} = 85\%$, $RoC = 50$ mm.	33
Figure A-5. Laser output power at 1645 nm of the resonantly diode cladding-pumped at 1532 nm Er(1%):YAG-core, channel waveguide laser versus the absorbed pump power. Maximum slope efficiency of $\sim 56.6\%$ was achieved with the output coupler reflectivity of 85%.	34
Figure A-6. Far field intensity distribution of the double-clad, channel waveguide Er:YAG laser. Left: 35 mm-long plano-concave laser cavity, $RoC = 50$ mm, $R_{OC} = 85\%$, $P_{PUMP} = 98$ W, $P_{OUT} = 25.4$ W, divergence ~ 13.4 mrad. Right: slightly misaligned, 110 mm-long, plano-concave laser cavity, $RoC = 100$ mm, $R_{OC} = 70\%$; $P_{PUMP} = 70$ W, $P_{OUT} = 8$ W, divergence ~ 6 mrad.	35
Figure A-7. The output power of the Er:YAG channel waveguide laser operated at 1617 nm versus the incident pump power. Wavelength selective laser resonator: $L_{CAV} = 35$ mm, $R_{OC} = 62\%$ at 1617 nm, $R_{OC} = 21\%$ at 1645 nm.	36
Figure B-1. (Color online) (a) Experimental layout of the Er:YAG-core channel waveguide laser pumped by a single-mode Er-fiber laser. (b) Optical layout used for simultaneous measurements of the incident and transmitted pump power along with the laser output power.	41
Figure B-2. (a) CW output power of the resonantly pumped Er:YAG-core waveguide laser versus the incident pump power and (b) CW output power versus the absorbed pump power. Laser cavity: length $Z = 41.3$ mm, $R_{OC} = 80\%$, $RoC = 50$ cm. With this R_{OC} the laser exhibited a dual wavelength operation, at 1617 and 1645 nm simultaneously.	42
Figure B-3. (Color online) Er:YAG channel waveguide laser beam radius (squared) at $1/e^2$ level as a function of the imaging plane position near the focal plane of the lens $f = 150$ mm. Solid squares – experimental data points, red line – hyperbolic fit to data.	43

List of Tables

Table 1. Samples and their measured refractive index differences (between the two materials in each pair) and absorptions. Typically, two measurements were made per sample.	8
Table 2. Refractive index difference (vs. undoped YAG) and absorption coefficient of RE-doped YAG.	9
Table 3. Comparison of measured and calculated Δn between YAG and spinel.	14
Table 4. Large surface orientations, using $<111>$ as a reference, measured at several places. δ and γ represent tilt angles from that reference in two orthogonal directions.	19
Table 5. Side surface orientations, using $<321>$ as a reference, measured at three places. δ and γ represent tilt angles from that reference in two orthogonal directions.	19
Table 6. Large surface orientation to reference $<310>$. δ and γ represent tilt angles from that reference in two orthogonal directions.	22

Acknowledgments

We gratefully acknowledge financial support from the High Energy Lasers Joint Technology Office for much of this work.

Summary

Conventional (silica-glass based) fiber lasers offer excellent advantages in beam quality and efficiency for high power lasers, but their material composition (glass) poses significant disadvantages in low pump absorption, gain, and thermal conductivity. All-crystalline fiber lasers, particularly if double-clad to facilitate diode pumping, would improve all these properties so as to enable much shorter length for a given power level, greatly facilitating power scaling. Yet, progress in fabrication of all-crystalline fibers has been limited thus far.

To investigate how to use such structures to best advantage, the U.S. Army Research Laboratory (ARL) in partnership with Onyx Optics undertook a High Energy Lasers Joint Technology Office (HEL-JTO)-funded study of fully crystalline waveguides with similar to conventional fibers double-clad geometry that can be fabricated (at moderate but useful lengths) using current bonding techniques. We have measured the refractive index of doped and undoped single-crystalline yttrium aluminum garnet (YAG) ($Y_3Al_5O_{12}$) and of ceramic spinel (magnesium aluminum spinel [$MgAl_2O_4$]) to determine the parameters for erbium (Er) (or thulium [Tm]):YAG/YAG/spinel double-clad waveguides with a single-mode Er (or Tm):YAG core. We also investigated YAG doped with ytterbium (Yb), optically inactive at the wavelengths relevant for resonantly pumped Er or Tm lasers, as an inner cladding material, as its index can be adjusted to facilitate design of a single-mode core with large area. We have characterized the thermal conductivity of each material, finding it to be much larger than that of glass, as expected. Finding one of the spinel samples to have an unusually large thermal conductivity, we studied it by x-ray diffraction and microscopy, concluding that it is probably a single crystal rather than a ceramic. Another spinel sample, which was definitely ceramic, thus gave a better test of the performance to be expected with a ceramic cladding with a crystalline YAG core and inner cladding.

We have undertaken laser experiments on both single- and double-clad Er:YAG cores of different sizes, and have obtained very encouraging world's-first and world-record laser performance. This includes 25-W continuous wave (CW) output due to cladding-pumping of what we believe to be the first truly double-clad all-crystalline YAG waveguide laser, and a record room-temperature slope efficiency (with respect to absorbed pump) of nearly 93% with excellent beam quality from a core-pumped waveguide with approximately $3800 \mu m^2$ cross-sectional area. Unfortunately, this project was not funded for Year 2, so the planned extension to greater lengths and thin enough cladding to be coilable could not be carried out.

INTENTIONALLY LEFT BLANK.

1. Introduction

Eye-safe lasers and, specifically, eye-safe fiber lasers are one of the key challenge areas in current high power laser development. Realistic analysis of Er-doped fiber laser power scaling indicates that the heat generation associated with pumping is still sufficiently detrimental that the fibers may reach fracture limits before nonlinear scaling limits (1, 2). Recent successes with resonantly pumped Er:YAG bulk solid-state lasers (3, 4) as well as Yb-free, Er-doped fiber lasers (5, 6) point to significant advantages of direct resonant pumping in minimizing heat deposition. Nevertheless, laser materials with much higher thermal conductivity than glass and better spectroscopy than that of rare-earth (RE) ions in glass (e.g., an order of magnitude higher absorption and emission cross sections), are required. So, there is increasing interest in real (i.e., coilable, not just “stiff thin rod” type, and double-clad) RE-doped “fibers” made of *crystalline* laser materials (single-crystalline or low-loss polycrystalline). A few scientific groups in Taiwan, Japan, and the United States (7) are trying to produce RE or transition metal doped *crystalline fibers*, but no tangible success has been reported so far. We report here the results of an effort aimed at the development of crystalline Er³⁺-doped and Tm³⁺-doped YAG double-clad fibers with non-circular, but rather ultra-thin planar waveguide geometry, coilable crystalline fiber (CCF), for eye-safe lasers and their scalability potential demonstration. ARL partnered with Onyx Optics, using Onyx’s Adhesive-Free Bond (AFB)® technology to fabricate the required double-clad CCF structures for this proof-of-concept effort.

1.1 Rationale

The rationale for using a RE-doped CCF is based on its high potential for achieving a few important properties toward efficient power-scalable performance with high beam quality: (1) much higher absorption cross section compared to glass fiber, so one can use much shorter fibers—thus significantly mitigating nonlinearity issues, (2) much higher thermal conductivity compared to glass combined with the large surface area-to-volume ratio typical of fibers, and (3) simplified high-intensity in-band pumping with diode-arrays using the “rectangular” structures described here. Indeed, in light of the latest detailed analysis of ultimate power scaling of diffraction limited fiber lasers and amplifiers, a notional Yb-doped YAG fiber laser shows ~10 times greater ultimate scaling potential than a Yb-doped silica-based fiber laser (16.9 kW vs. 1.89 kW, as shown in figure 1) (8). Originally this analysis was developed by Lawrence Livermore National Laboratories (LLNL) for Yb-doped silica-based fiber lasers only (9), but recently it was extended to analyze a much wider range of materials, including a notional crystalline YAG fiber (8). Based on this analysis, development of double-clad crystalline fiber structures, even though a challenging task, if successful, can lead to a major leap in fiber laser power scaling out of a single aperture, about an order of magnitude! The question remains: can crystalline fibers with dimensions acceptable for use in fiber lasers be flexible enough to be

“coilable” (which is a stringent requirement for fibers intended for fieldable fiber lasers)? Onyx Optics carried out a 5-year Congressional interest program under the oversight and collaborative involvement of ARL, which significantly advanced their capabilities toward military applications. We believe that the CCF fabrication risks and its coilability issue are largely mitigated by a recent demonstration of a flexible YAG strip with dimensions of $50 \mu\text{m} \times 10 \text{ mm} \times 200 \text{ mm}$, which has shown to be *bendable* at least over a diameter of $\sim 30 \text{ cm}$ (figure 2).

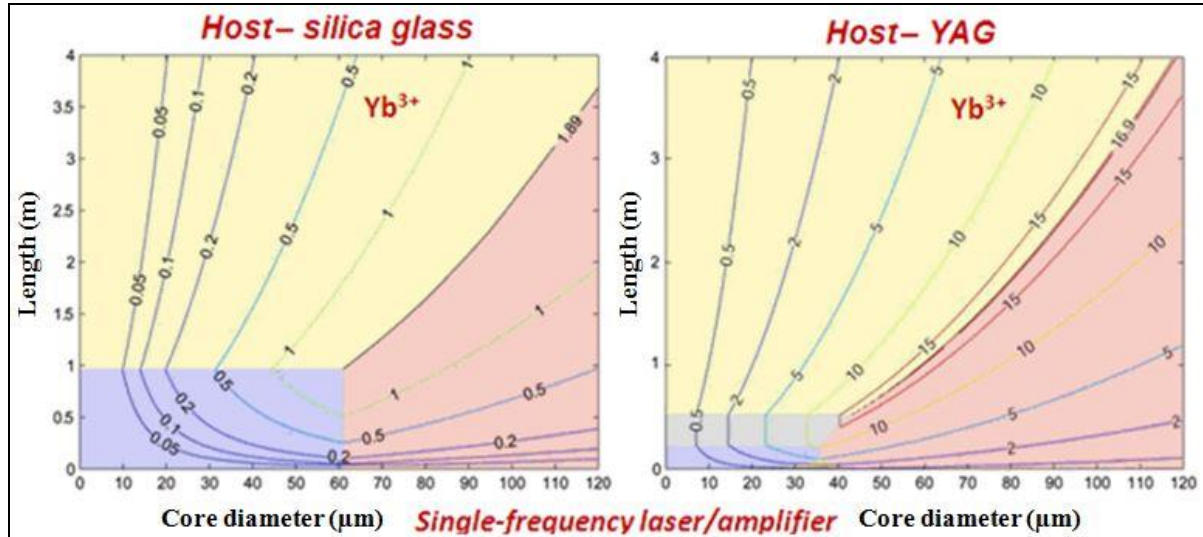


Figure 1. Contour plot of scalability of an Yb^{3+} -silica fiber vs. Yb^{3+} :YAG fiber laser in the single frequency laser/amplifier case. Contour lines are output power in kW. In the yellow region, the laser output power is limited by stimulated Brillouin scattering; in the pink region, the limit is thermal lensing in the waveguide; in the blue region, the limit is pump diode brightness; and in the gray region, the output power is damage-limited (8).

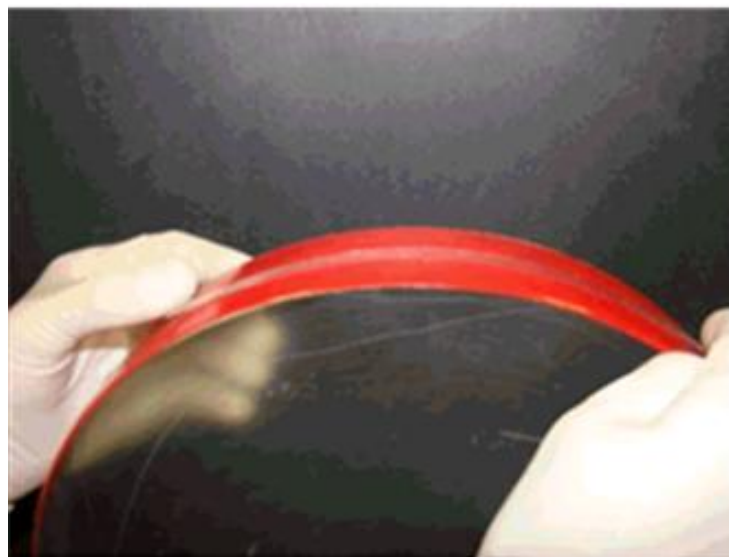


Figure 2. Flexible YAG strip of $200 \times 10 \times 0.047 \text{ mm}^3$, bent over a 300-mm-diameter optic.

Coilability of a YAG strip of assumed 450 MPa flexural strength (typical of single-crystalline YAG) has been estimated for 50- and 100- μm -thick strips. We predicted the minimum bending radius before breakage to be \sim 20 mm (figure 3) for the 50- μm -thick YAG strip and 150 mm for the 100- μm -thick strip. So, a \sim 30-cm-diameter bend for a 50- μm -thick strip, as shown in figure 2, is not much of a stretch at all. It means that the double-clad CCF with this thickness can be easily coiled into a 30-cm-diameter spool if it is required by a specific laser design.

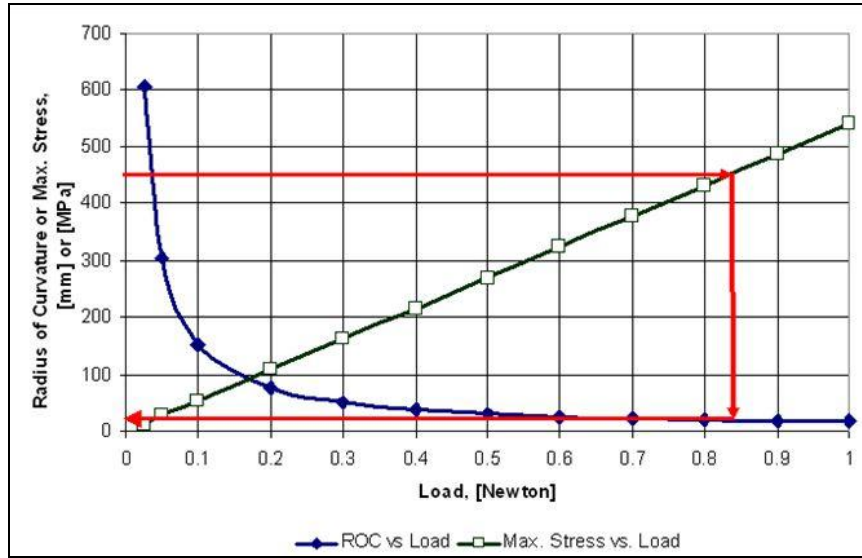


Figure 3. YAG strip of 50 μm thickness is predicted to have a minimum bending radius of \sim 20 mm before breakage. Red lines: The line at 450 MPa intersects the green curve to determine the maximum load; the resulting vertical line intersects the blue curve to determine the minimum radius of curvature, which can be read off by following the lower horizontal line.

1.2 Brief Review of Research Plan

In order to achieve project goals, our plan was to use AFB in Year 1 to manufacture low-loss 100–200 mm long, double-clad CCFs and planar waveguides with \sim 20 μm \times 20 μm and 20 μm \times 10 mm doped cores, respectively, clad with undoped YAG (or lutetium aluminum garnet [LuAG, $\text{Lu}_x\text{Y}_{1-x}\text{AG}_3$] or spinel). Figure 4 shows the cross section of a representative CCF design intended for the proof-of-concept experiments with clad-pumping. The CCF with a 20 μm \times 20 μm doped core is a modal analog of a standard large mode area (LMA) glass fiber, which means single-transverse-mode (STM) (TEM_{00}) laser output can be obtained by merely coiling the fiber. The outside of the CCF (the perimeter of the cross section in figure 4) can be coated with a low refractive index oxide layer such as alumina (Al_2O_3) or silica (SiO_2), functioning as a second cladding. Such a design enables both low-numerical aperture (NA) core pumping and high-NA cladding pumping for CCF laser testing. The spinel serves as a cladding material and shapes the aspect ratio to prevent kinks during the coiling of the CCF.

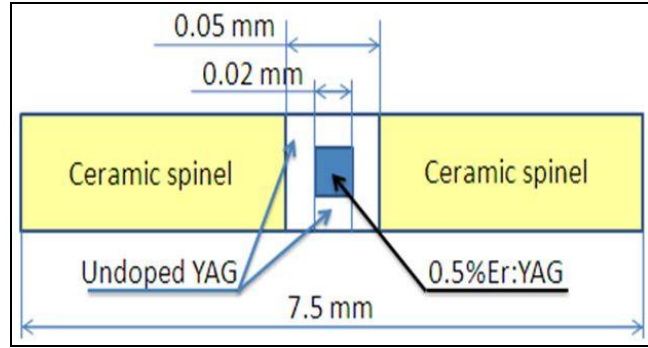


Figure 4. Simplified design of Year-1 CCF.

The second case, with $20 \mu\text{m} \times 10 \text{ mm}$ core, gives a rectangular core with much larger (~500 times) area—for significant power scaling. Although this design controls the beam quality in the $\sim 20 \mu\text{m}$ direction, it yields a heavily multimode shape in the “slow” direction. The Year 2 plan was to investigate a number of schemes to achieve single-mode output and high-power scalability for this planar waveguide design fiber. The AFB fabrication of the CCFs follows a process that has already been developed at Onyx Optics for crystalline waveguides, with the only difference being that the cladding layers are much thinner for CCFs.

1.3 Major Project Developments and Results

Our research had three clearly distinct parts to it:

1. One substantial part consisted in development of the AFB-based bonded doped/undoped YAG waveguiding parts (“AFB fabrication”) and their passive mechanical and thermal testing along the way—ongoing during the entire development process.
2. The second part was comprehensive bonded structure and mode simulation.
3. The third substantial part was comprehensive laser testing of all the parts, which also provided the necessary feedback to the fabrication process.

2. Development of the AFB-Based Bonded Doped/Undoped YAG Waveguiding Parts (Double-Clad Crystalline Fibers)

Refractive index measurements as a function of Er^{3+} and Tm^{3+} concentration in YAG, versus undoped and Yb-doped YAG were conducted to get the required waveguide design parameters. Yb:YAG is a useful alternative to undoped YAG as a cladding material because variation of its index with Yb concentration enables finer control of the NA.

2.1 Refractive Index Measurement Samples

Bonded doublets have been prepared for refractive index measurements of composite dimensions of $\sim 10 \times \sim 10 \times \sim 5$ mm, with 10x10 mm and 10x5 mm surfaces precision polished parallel to ~ 10 s using several available doped and undoped YAG crystals, and Δn is measured without relying on the nominal concentration of either member of the doublet. The combinations are shown in figure 5.

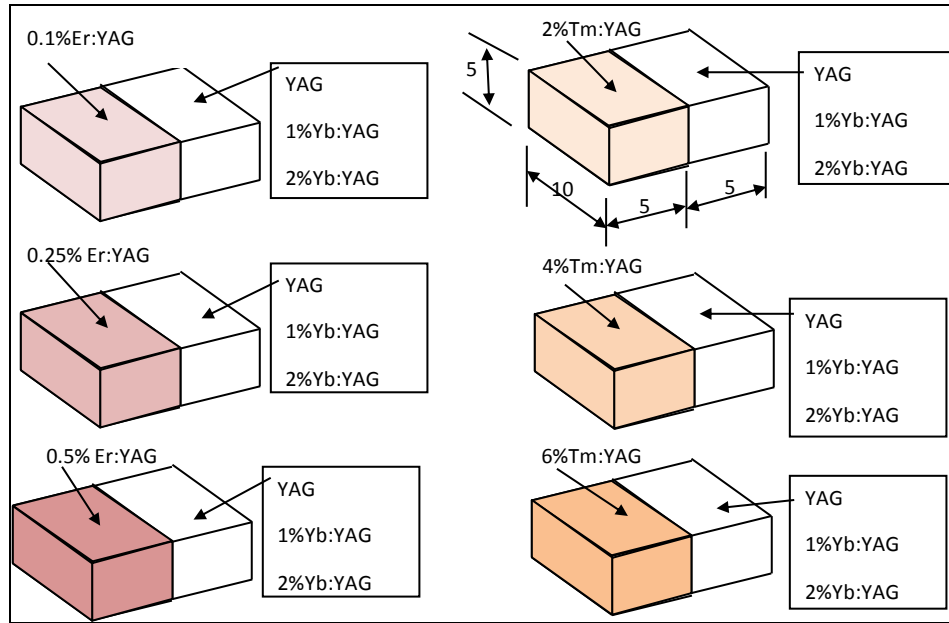


Figure 5. Doublet designs for refractive index measurements. Dimensions are in mm.

2.2 Refractive Index Results

Refractive index changes of RE-doped YAG samples have been measured using a Zygo VeriFire MST 1550 nm interferometer. Theoretical accuracy of the measurements can be determined from $\Delta n = \Delta \text{OPD}/d$. For the ΔOPD measurement with an error ± 10 nm, the accuracy of the refractive index difference measurement will be 1×10^{-6} for the 10 mm thick samples; 2×10^{-6} for the 5 mm thick samples; and 3.3×10^{-6} for the 3-mm thick samples.

Several samples have been prepared for the refractive measurement. The results have been listed in tables 1 and 2, and are also shown in figures 6–8.

Table 1. Samples and their measured refractive index differences (between the two materials in each pair) and absorptions. Typically, two measurements were made per sample.

Sample	Dimensions (mm ³)	Δn to YAG (10 ⁻⁴)	Absorption coefficient α (cm ⁻¹)
0.1%Er:YAG /YAG, sample A	3.053×5.054×4.04	0.184 0.2025	0.211@1532
0.1%Er:YAG /YAG, sample B	3.054×5.055×4.04	0.186 0.214	0.275@1532
0.1%Er:YAG /1%Yb:YAG	4.950×6.976×6.02	1.295 (Yb) 1.20 (Yb)	0.25@1532 (Er) 0.96@941 (Yb) 0.953@969 (Yb)
0.1%Er:YAG /2%Yb:YAG	4.788×7.017×6.05	3.054 (Yb) 3.014 (Yb)	0.24@1532 (Er) 1.85@941 (Yb) 1.92@969 (Yb)
0.5%Er:YAG /YAG, sample A	5.038×10.042×10.04	1.128 1.168	1.43@1532
0.5%Er:YAG /YAG, sample B	5.038×10.044×10.04	1.15 1.147	1.443@1532
0.5%Er:YAG /1%Yb:YAG, sample A	5.050×10.047×10.01	1.26 (Yb) 1.22 (Yb)	1.414@1532 (Er) 1.011@941 (Yb) 0.966@969 (Yb)
0.5%Er:YAG /1%Yb:YAG, sample B	5.048×10.048×10.01	1.244 (Yb) 1.196 (Yb)	1.465@1532 (Er) 0.98@941 (Yb) 0.97@969 (Yb)
0.5%Er:YAG /2%Yb:YAG, sample A	5.052×10.022×10.05	3.033 (Yb) 3.019 (Yb)	1.449@1532 (Er) 1.933@941 (Yb) 1.946@969 (Yb)
0.5%Er:YAG /2%Yb:YAG, sample B	5.054×10.023×10.05	3.066 (Yb) 3.038 (Yb)	1.461@1532 (Er) 1.885@941 (Yb) 1.979@969 (Yb)
2%Tm:YAG /YAG	5.046×5.734×5.61	3.541 3.645	2.12@786 1.839@781 0.446@793 0.397@798 0.348@805

Table 2. Refractive index difference (vs. undoped YAG) and absorption coefficient of RE-doped YAG.

Dopant	$\Delta n (10^{-4})$ per % at 1550 nm	$\alpha (cm^{-1})$ per %
Er	2.1	2.8 at 1532 nm
Yb	1.6	1.06 at 969 nm
Tm	2.08	0.997 at 786 nm

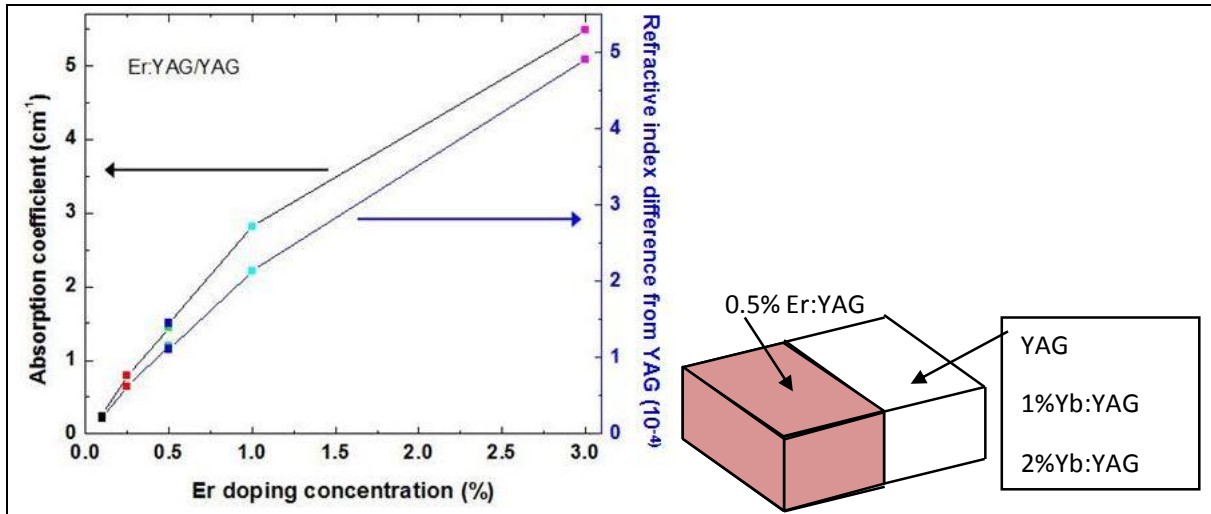


Figure 6. Absorption coefficient at 1532 nm and refractive index changes at 1550 nm of Er-doped YAG vs. doping concentration. Neglecting the results measured from the 3%Er:YAG, the fitted refractive index change is $2.1 \times 10^{-4}/\%$; absorption coefficient is $2.8 \text{ cm}^{-1}/\%$.

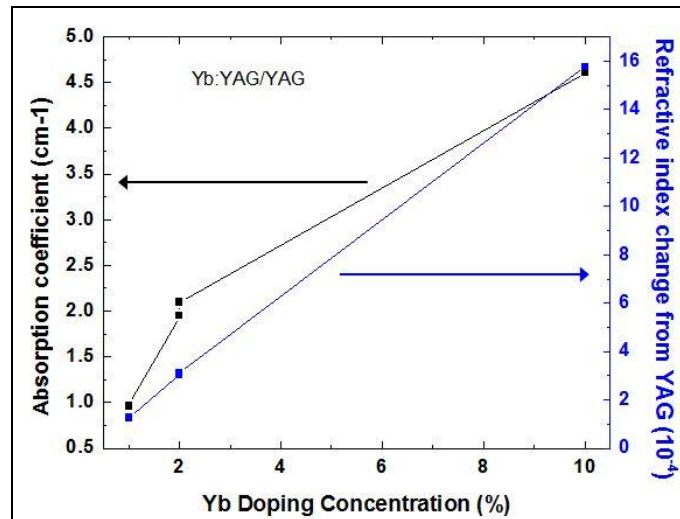


Figure 7. Absorption coefficient at 969 nm and refractive index changes at 1550 nm of Yb-doped YAG vs. doping concentration. Neglecting the absorption measured from the 10%Yb:YAG, the fitted refractive index changes is $1.6 \times 10^{-4}/\%$; absorption coefficient is $1.06 \text{ cm}^{-1}/\%$.

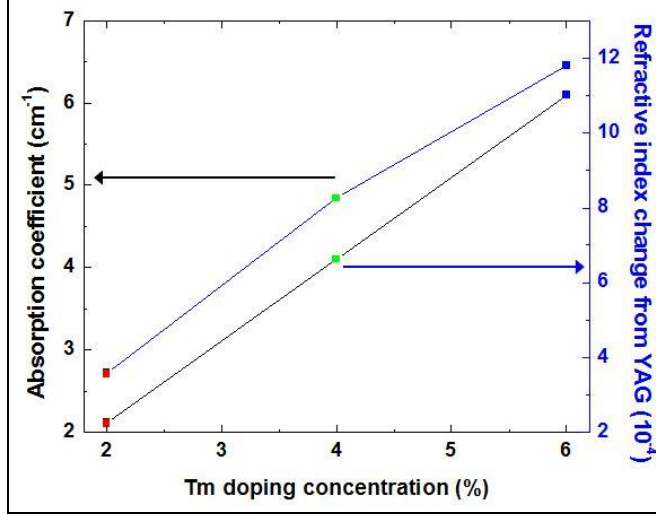


Figure 8. Absorption coefficient at 786 nm and refractive index changes at 1550 nm of Tm-doped YAG vs. doping concentration. The fitted refractive index change is $2.08 \times 10^{-4}/\%$; absorption coefficient is $0.997 \text{ cm}^{-1}/\%$.

The average refractive index differences are $1.236 \times 10^{-4} \pm 3.8 \times 10^{-6}$ for Er:YAG versus 1% Yb:YAG and $3.037 \times 10^{-4} \pm 2.0 \times 10^{-6}$ versus 2% Yb:YAG. One can see that the standard deviations in the measured data are consistent with the estimates made at the beginning of this section. A summary of the refractive index differences and absorption coefficients, each per atomic percent of dopant, is listed in table 2.

3. Mode Simulation of Tm:YAG Double-Clad Waveguide Structures

3.1 Numerical Aperture (NA)

The purpose of this part of the work is to provide a general view of the mode distribution inside AFB square core waveguide structures to guide our waveguide and laser designs.

The Tm:YAG waveguide structure used in the mode simulation is illustrated in figure 9. It consists of Tm:YAG square core, undoped YAG inner cladding and spinel outer cladding. Using the refractive index difference results for Tm:YAG from table 2, the NAs have been calculated and listed below for the proposed 2% and 4% Tm:YAG waveguide structures, and for the inner cladding:

- $\text{NA}_{2\% \text{Tm:YAG}} = 0.039$
- $\text{NA}_{4\% \text{Tm:YAG}} = 0.055$
- $\text{NA}_{\text{inner}} = 0.64$

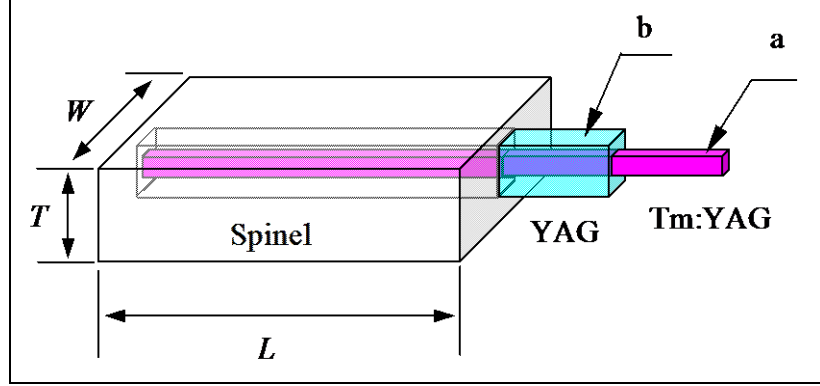


Figure 9. Schematic illustration of double-clad Tm:YAG waveguide-fiber structure. The structure uses un-doped YAG as inner cladding and spinel as outer cladding. The design is for laser diode cladding-pumped 2- μm crystalline waveguide Tm:YAG laser.

3.2 Single-Mode Condition

For square (or rectangular) waveguide structures, we can define a normalized frequency B-number (10, 11) that is similar to the V-number in fiber optics.

$$B = \frac{ka}{\pi} NA_{core} \quad (1)$$

Here k is the wave number corresponding to the frequency of the light and a is the width of the waveguide. Usually for a square core waveguide, single-mode waveguiding requires $B < 1.37$ (10, 11). Based on this criterion, the single-mode waveguide width will be the following:

- $a < 35 \mu\text{m}$ for 2% Tm:YAG;
- $a < 25 \mu\text{m}$ for 4% Tm:YAG.

For other Tm doping concentrations, one may use figure 10 to find out the single-mode square core width.

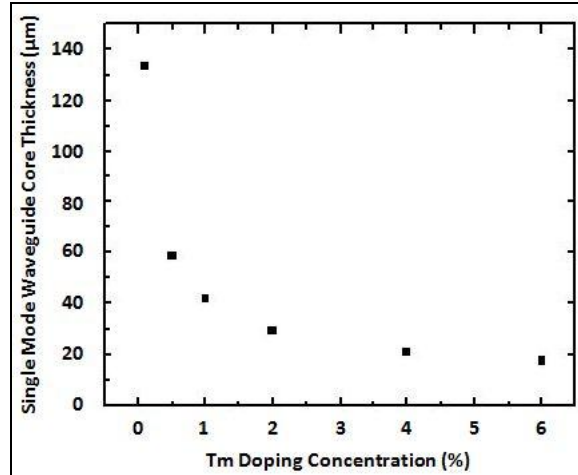


Figure 10. Theoretical single-mode waveguide core width as a function of Tm doping concentration.

3.3 Mode Intensity Distribution

For the ongoing research project, the designed waveguide core width is 20 μm and 28 μm for the 4% and 2% Tm:YAG, respectively. Therefore, both structures are single-mode waveguides. The intensity distribution of the fundamental mode is calculated with Marcatili's method (1) and plotted in figures 11–14. Even though we have square waveguide core, the fundamental waveguide mode is still round and Gaussian-like as shown in figures 11 through 14.

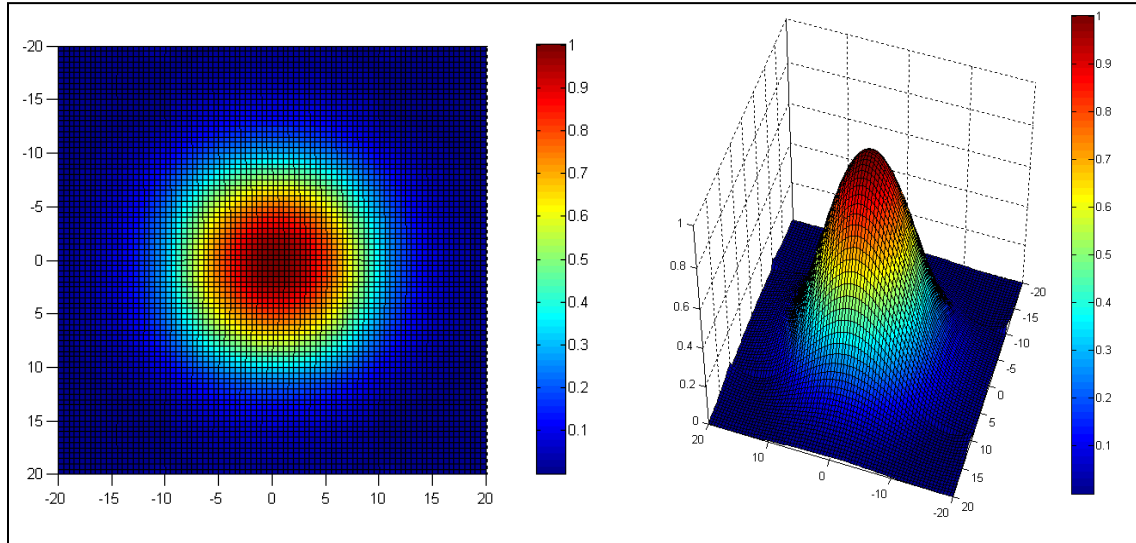


Figure 11. Simulated two-dimensional (2-D) and three-dimensional (3-D) field distributions inside the 4%Tm:YAG square core waveguide with core width of 20 μm .

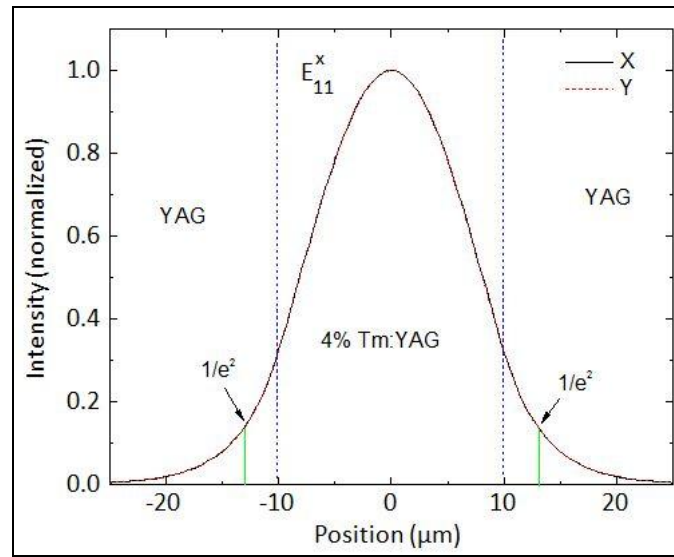


Figure 12. Field distributions along x- and y-axis (identical).
Fundamental mode radius is $\sim 13.1 \mu\text{m}$ at $1/e^2$.
Mode area is around $\sim 539 \mu\text{m}^2$.

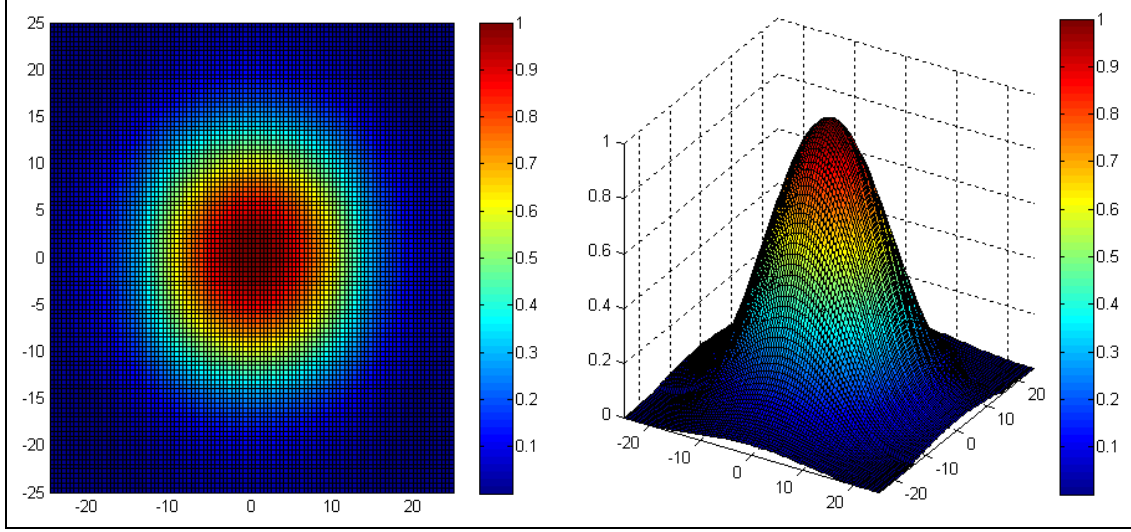


Figure 13. Simulated 2-D and 3-D field distributions inside 4%Tm:YAG square core waveguide with core width of 28 μm .

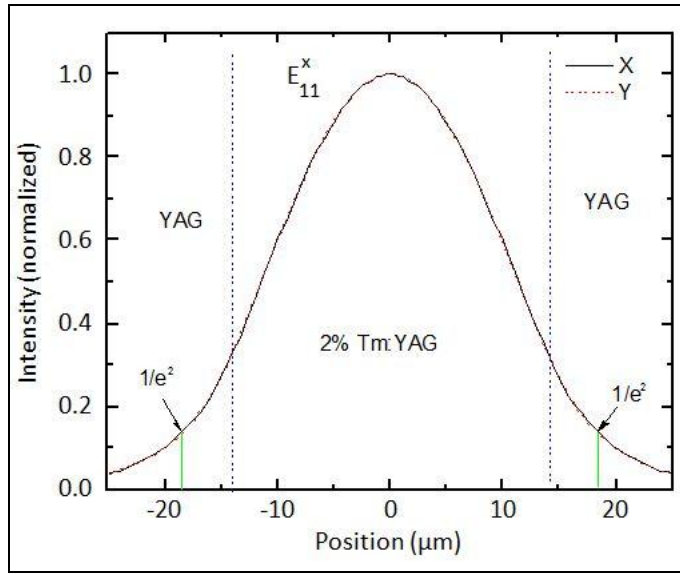


Figure 14. Field distributions along x- and y-axis (identical) of 2%Tm:YAG waveguide. Mode radius is $\sim 18.4 \mu\text{m}$ at $1/e^2$. Mode area $\sim 1060 \mu\text{m}^2$.

The calculations indicate that LMA single-mode waveguides can be fabricated with AFB technology, even though the AFB waveguide-fiber can only have square core, due to the limitations of the fabrication process. The fundamental mode is still round and Gaussian-like distributed. The fundamental mode diameter, which is based on our simulations in the 2% and 4% Tm:YAG waveguide, is about 1.31 times of the waveguide width.

4. Thermal Conductivity of Ceramic Spinel (To Be Used As Outer Cladding)

In this AFB fiber project, ceramic spinel was the selected outer cladding material of the AFB double-clad waveguide-fiber structures. The refractive index difference between the YAG and the spinel determines the NA of the inner cladding. The thermal conductivity of spinel will directly affect the performance of the proposed AFB fiber lasers.

In order to precisely measure the refractive index and the thermal conductivity of the ceramic spinel, two AFB spinel-YAG composites were produced and measured by an interferometric method (12).

4.1 Sample

The AFB spinel-YAG sample design is illustrated in figure 15.

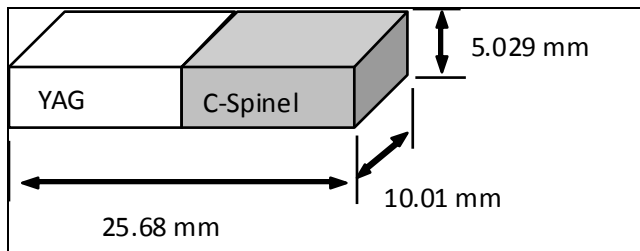


Figure 15. Schematic illustration of AFB spinel-YAG composite used in the interferometric measurement.

To check the refractive index difference, the sample's optical path difference (OPD) was measured on both the YAG and spinel sides. The measured results have been listed in table 3.

Table 3. Comparison of measured and calculated Δn between YAG and spinel.

Material	OPD (mm)	d (mm)	Δn to YAG	Calculated
YAG	9.184	5.029	—	—
Spinel	8.622	5.029	0.11175	0.11235

According to our measurement, the numerical aperture of the inner cladding is calculated to be around 0.64.

4.2 Thermal Conductivity

In order to measure the thermal conductivity, the coefficient of thermal expansion (CTE) for OPD needs to be measured first. Figure 16 is the plot of the measured OPD increase as a

function of temperature. From figure 16 one can determine that for spinel, $\gamma=2.43\times10^{-5}\text{ }^{\circ}\text{C}^{-1}$. The γ determined for YAG from figure 17 is about $2.2\times10^{-5}\text{ }^{\circ}\text{C}^{-1}$.

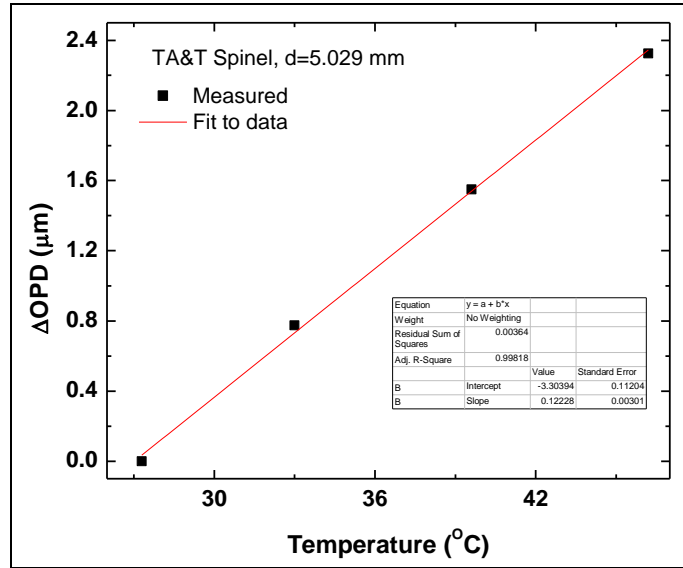


Figure 16. OPD changes as a function of temperature for TA&T-manufactured ceramic spinel (C-spinel).

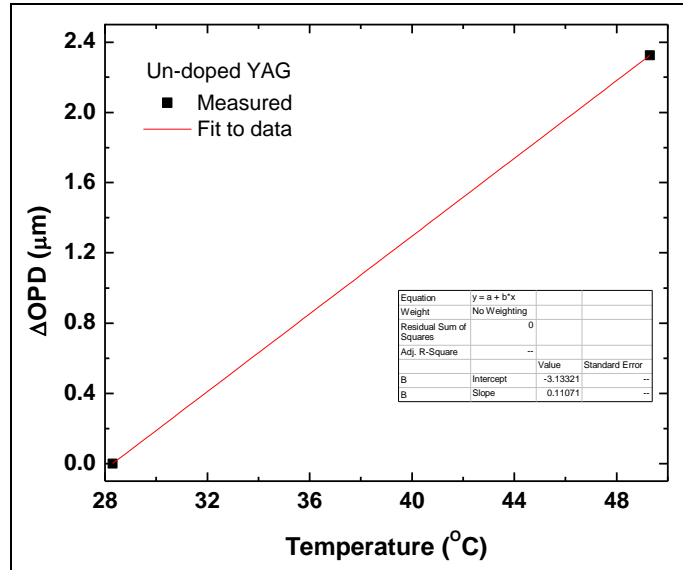


Figure 17. OPD changes as a function of temperature for undoped YAG.

For the thermal conductivity measurement, one end of the spinel-YAG sample is attached with a heater with a heat power of 0.32 W. The other end of the sample is contacted with a water-cooled heat sink. At a steady state, the sample temperature distribution can be determined by OPD changes and the thermal conductivity can be determined by equation 2:

$$K_{YAG} \frac{dT_{YAG}}{dx} = K_{Spinel} \frac{dT_{Spinel}}{dx} \quad (2)$$

Figures 18 and 19 are the measured relative temperature distributions inside the spinel and the YAG for the two samples, denoted Samples #1 and #2.

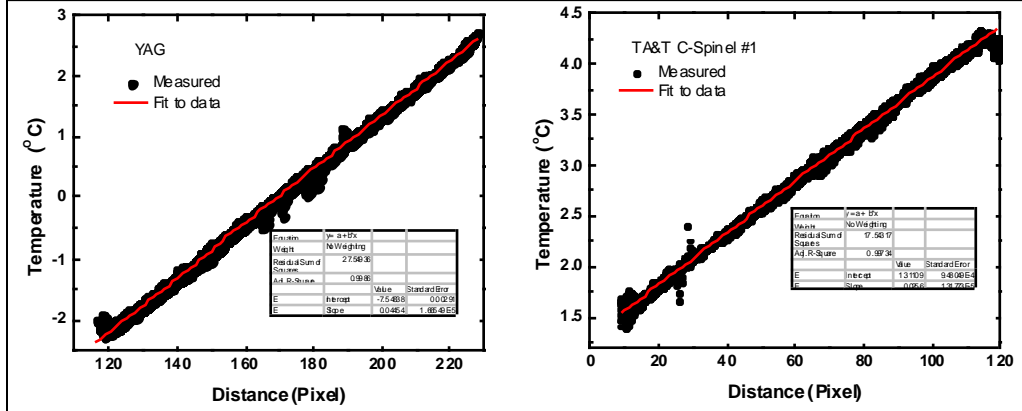


Figure 18. Temperature as a function of distance inside the YAG and spinel portions of Sample #1.

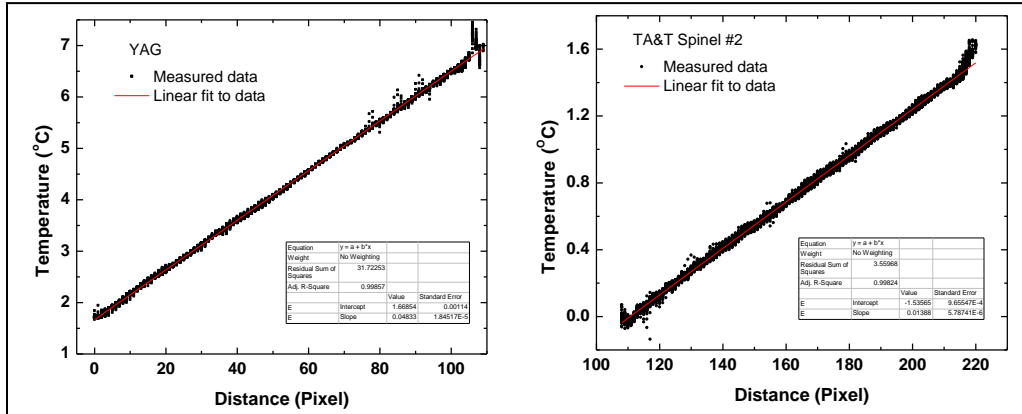


Figure 19. Temperature as a function of distance inside the YAG and spinel portions of Sample #2.

By using $K_{YAG}=13.4 \text{ W/m}\cdot\text{K}$ (13) as a reference, K_{spinel} is determined to be $\sim 23.7 \text{ W/m}\cdot\text{K}$ for Sample #1 and $46.7 \text{ W/m}\cdot\text{K}$ for Sample #2. Both numbers are much higher than the previous value reported for ceramic spinel ($16 \text{ W/m}\cdot\text{K}$) (13). As is discussed in a later section, Sample #2 preliminarily has been determined by x-ray analysis to be a single crystal.

4.3 Interface Heat Transfer Coefficient

Figure 20 is the full temperature distribution inside Sample #2. The temperature step at the YAG/spinel bonding interface is about $0.055 \text{ }^{\circ}\text{C}$. The interface's heat transfer coefficient that can be determined by equation 3 is about $0.997 \times 10^5 \text{ W}\cdot\text{m}^{-2}\cdot\text{}^{\circ}\text{C}^{-1}$.

$$H = \frac{K_{YAG}}{\Delta T_{int}} \frac{dT_{YAG}}{dx} \quad (3)$$

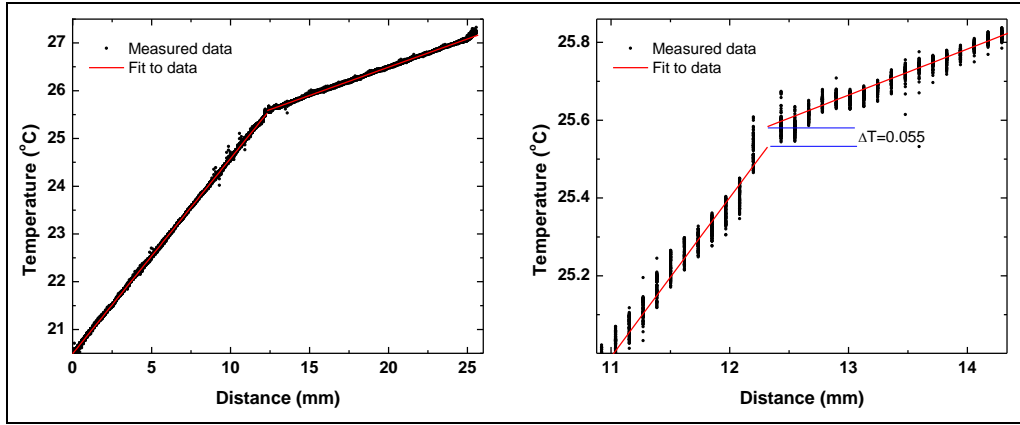


Figure 20. Temperature distribution inside Sample #2. Left: full sample. Right: detail around the interface.

4.4 Possible Thermal Issues with TA&T Spinel

As seen in figure 20, extremely high thermal conductivities have been reported in spinel samples from TA&T (our sole source for ceramic spinel for the bulk of this project). One sample has a measured thermal conductivity of 46.7 W/m·°C, which is 2 to 3 times higher than the supplier and the literature data (13–15). To investigate the difference between the high thermally conductive spinel and the other sample, we have measured the x-ray diffraction spectrum of the spinel samples. Our results indicate that the high thermally conductive spinel is at least highly oriented ceramic if it is not a single crystal.

4.4.1 X-Ray Diffraction Spectrum

Figure 21 shows a schematic of the TA&T spinel sample and positions used for the x-ray measurements.

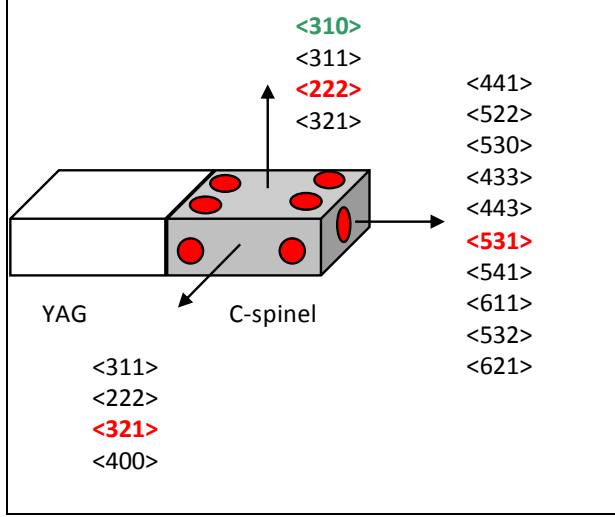


Figure 21. Schematic illustration of the TA&T spinel sample and the positions used for X-ray measurements (red dots). For each face, the three-integer symbols indicate candidate crystallographic directions that were considered, and the symbols in red denote the orientations that best fit the data. For the large face, the green symbol indicates the reassigned direction discussed in the text.

Large surfaces: Sample orientation has been measured at four corners of the top surface and two of the under surface. X-ray peaks have been measured around 5.31, 10.62, and 15.9 keV. The typical x-ray spectra of the large surface are shown in figure 22. Four possible lattice orientations have been checked for the large surface. Among them, $<222>$ gives the best fit. The measured $<222>$ directions from the surface normal for the six points have been listed in table 4. However, if the 5.31 keV peak assigned to $<222>$, we should see a $<111>$ peak at about 2.65 keV that is not observed in the x-ray spectrum.

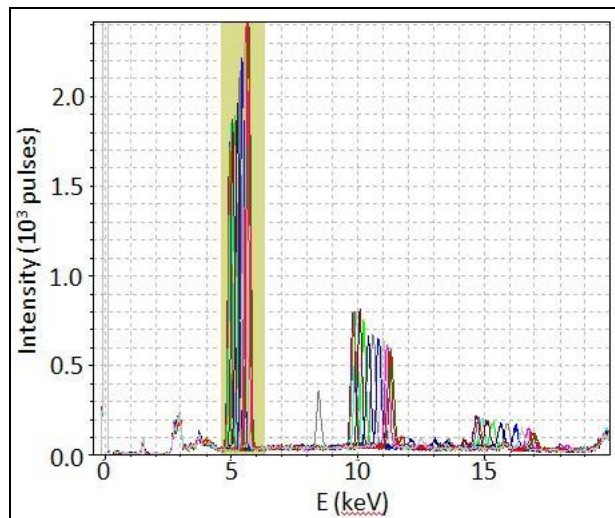


Figure 22. Typical x-ray spectra measured at several spots on the large spinel surfaces. The shaded region highlights the 5.31 keV region discussed in the text.

Table 4. Large surface orientations, using $<111>$ as a reference, measured at several places. δ and γ represent tilt angles from that reference in two orthogonal directions.

Position	δ (°)	γ (°)
1	2.316 (0.141)	-156.93 (3.564)
2	2.264 (0.141)	-158.698 (3.633)
3	2.31 (0.140)	-155.938 (3.55)
4	2.339 (0.139)	-159.100 (5.465)
5	2.224 (0.139)	-19.125 (flipped)
6	2.254	-18.879 (flipped)

From table 4, one can see that within the estimated uncertainties, all the measured positions have the same orientation.

Side surfaces: Two points on the front side and one on the back side have been measured. X-ray peaks are around 5.79, 11.6, and 17.5 keV. The typical x-ray spectra of the side surface are shown in figure 23 and the results have been listed in table 5. Within the measured error range, all the three points have the same orientation. The best-fit lattice direction is $<321>$.

Table 5. Side surface orientations, using $<321>$ as a reference, measured at three places. δ and γ represent tilt angles from that reference in two orthogonal directions.

Position	δ (°)	γ (°)
1	0.651 (0.095)	11.575 (8.359)
2	0.681 (0.099)	12.305 (8.354)
3	0.811 (0.099)	171.685 (7.020) (flipped)

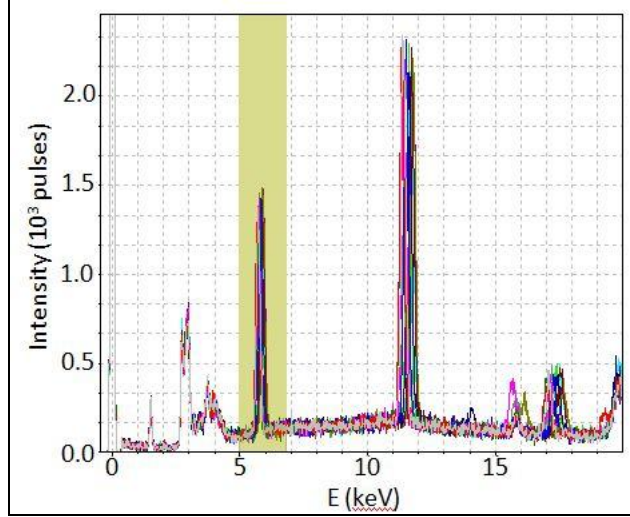


Figure 23. Typical x-ray spectra measured at several spots on the side spinel surfaces. The shaded region highlights the 5.31 keV region discussed in the text.

End surface: One point has been measured and plotted in figure 24 with one major x-ray peak group around 9.1 keV. The best fit orientation is $\langle 531 \rangle$ with $\delta=1.693^\circ$ (0.010) and $\gamma=125.278^\circ$ (0.357).

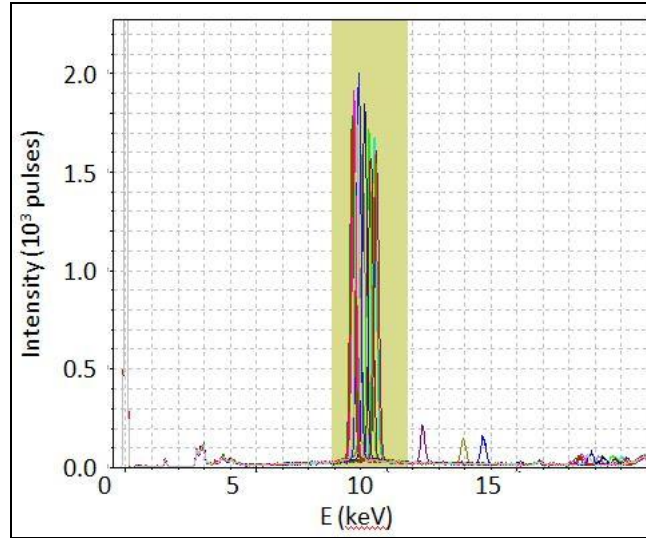


Figure 24. X-ray spectra (several scans) on the end spinel surface. The shaded region highlights the 9.1 keV region noted in the text.

4.4.2 NewView Microscope Images

The sample surfaces were checked with Zygo NewView microscope at different locations. No spinel grain has been observed at any randomly selected check point. Figure 25 shows typical NewView images taken from three surfaces of the sample.

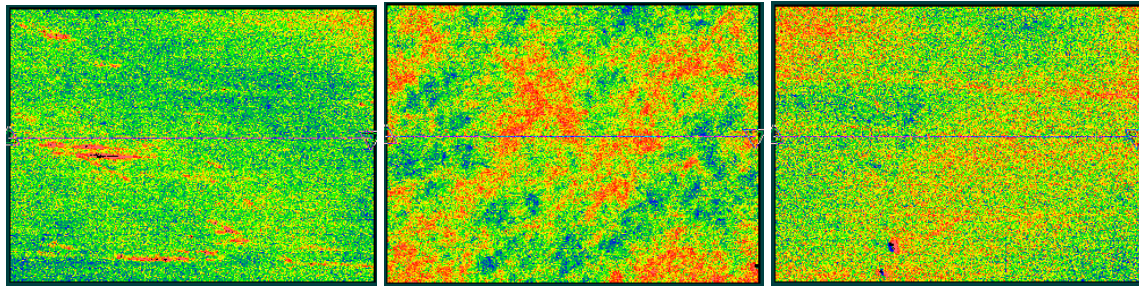


Figure 25. NewView microscope image taken from the large, side and end surfaces of the TA&T high thermal conductivity spinel. (By contrast, see figure 27, which has clear evidence of grain structure.)

All the above measurements are consistent with the TA&T highly thermally conductive sample being a single spinel crystal, or perhaps a ceramic with all grains strongly aligned. However, the three best fitting orientations $<222>$, $<321>$, and $<531>$ cannot form a Cartesian coordinate system even though any two of the three direction groups can be perpendicular. For this reason we reassigned the sample large surface to $<310>$. Table 6 is the list of the orientation angles of the six measured points of the sample's large surfaces after reassigned the surface orientation. The possible sample orientation has been plotted in figure 26. The fact that an orientation has been identified that is reasonably consistent with all observations strengthens the case that this highly thermally conductive sample is actually a single crystal. If so, the absence of grain boundaries to cause scattering provides a partial explanation of its high conductivity.

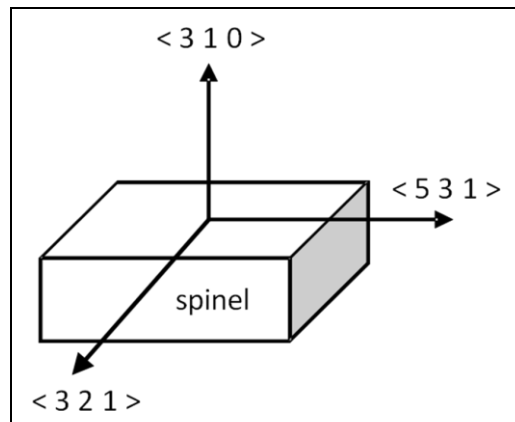


Figure 26. Refined proposed crystal orientation of TA&T spinel.

Table 6. Large surface orientation to reference $<310>$. δ and γ represent tilt angles from that reference in two orthogonal directions.

Position	δ (°)m	γ (°)
1	3.270 (1.149)	-156.786 (20.891)
2	3.263 (1.151)	-155.798 (20.960)
3	3.302 (1.151)	-158.944 (20.728)
4	3.201 (1.153)	-158.538 (21.388)
5	3.318 (1.158)	-19.124 (21.878) (flipped)
6	3.179 (1.157)	-18.879 (21.589) (flipped)

4.4.3 Low Thermal Conductivity Spinel Samples

For the TA&T spinel with thermal conductivity of 23.7 W/m·°C, large size spinel grains can be observed clearly under NewView microscope, as shown in figure 27. X-ray measurements are shown in figure 28. No specific orientation can be assigned for any sample surface. As a comparison, x-ray spectra of a spinel obtained from MER are presented in figure 29. Note that it is much less clean than the spectra of figure 28, suggesting that even the low thermal conductivity sample of TA&T spinel may have a simpler grain structure than the MER spinel.

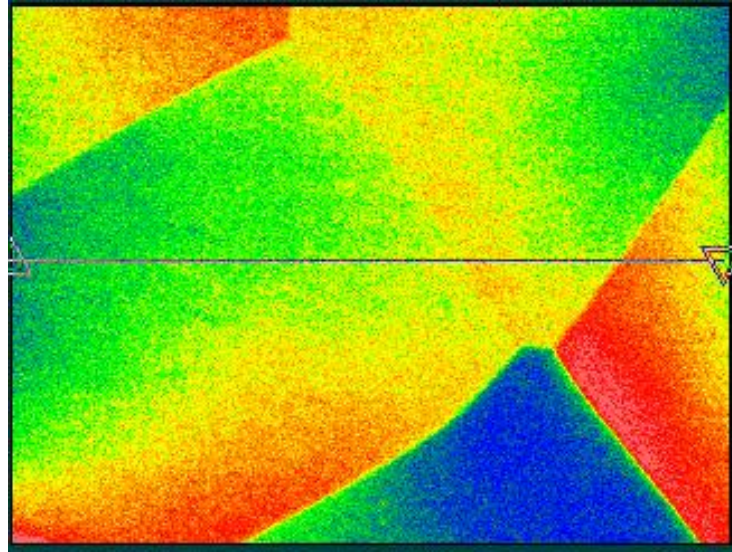


Figure 27. NewView image of the relative lower thermal conductive spinel sample. The image size are x=0.35 mm and y=0.27 mm.

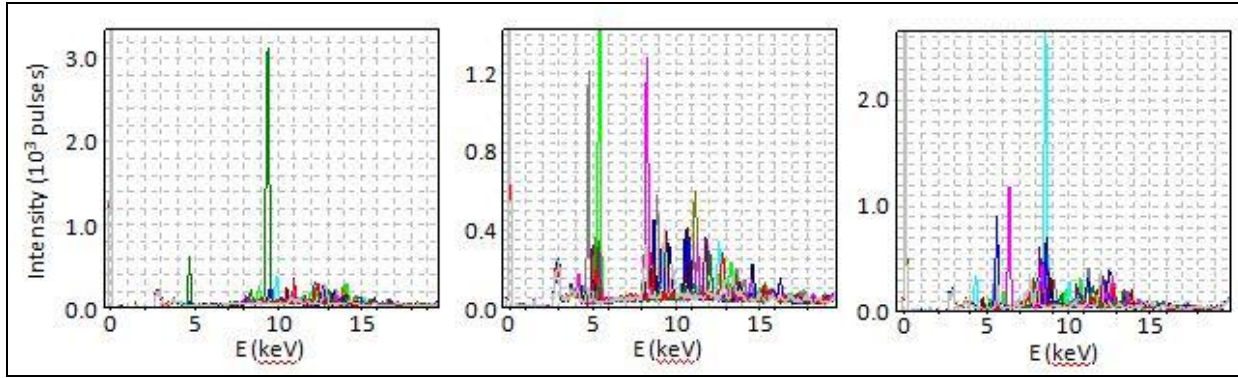


Figure 28. X-ray spectra of the low thermal conductivity TA&T spinel sample, for multiple spots on three faces, similar to those used in figures 21–24.

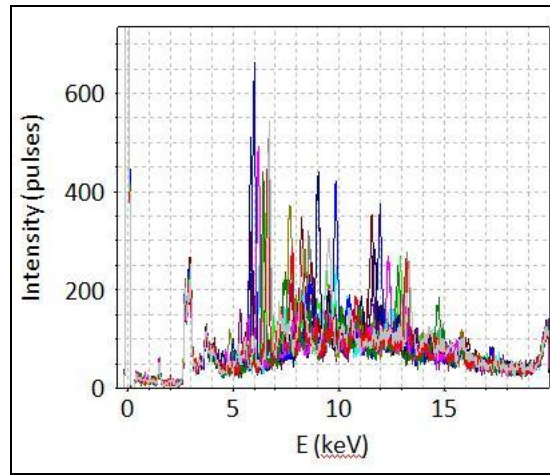


Figure 29. X-ray spectra of MER spinel taken at several spots.

5. Laser Experiments

During the course of this project, based on the material and AFB structure research, a few waveguides structures appropriate for lasers experimentation were fabricated and tested. None of these structures was as long as we originally anticipated. Due to serious difficulties in achieving proper quality of waveguide fabrication and achieving the required precision in parts' cross-sectional dimensions (which happens to be length dependent: the longer the part, the more difficult it is to achieve a few-micrometer accuracy in part fabrication), most of the laser work was carried out with waveguides that were 30–50 mm long. A significant number of parts of longer length have been partially fabricated—unfinished to one degree or another. These parts (which were actually meant to be advanced structures for the Year 2 work) could not be finished without Year 2 funding (which has not been awarded). Thus, they can be finished if additional funding is made available to Onyx Optics in the future one way or another. It is also worth

noting that the development of the proper double-clad and single-mode structures with laser demonstrations actually was a Year 1 goal, while the *coilable* structure development was intended to happen in Year 2.

We report our laser results by incorporating two of our publications as appendices. The laser experiments were performed on 30–50 mm long true Er:YAG-core double-clad and small-core Er:YAG true single-mode channel waveguides. These results were reported at the SPIE Defense and Security (Europe) 2012 in September 2012, managed by JTO, and at SPIE Defense, Security, Sensing (DSS) (Baltimore). They were also published in *Optics Express*, with at least one more submission planned to another journal. JTO's support was gratefully acknowledged.

The principal results are as follows. Using a large-core (500 μm x 500 μm) waveguide 30 mm long, pumping of the 700 μm x 700 μm inner cladding with a line-narrowed diode laser module, we achieved over 25 W of output power with 56% slope efficiency (relative to absorbed power) and a beam quality of $M^2 \sim 2.6$. Due to the very large core area, this beam quality was determined by the cavity mirrors. Refined cavity alignment improved the beam quality significantly, at the cost of substantially reduced output power. By core-pumping a waveguide with smaller core area (61.2 μm x 61.6 μm) and 41 mm length, we obtained over 9 W CW with nearly 93 % slope efficiency (relative to absorbed pump power) and excellent beam quality ($M^2 \sim 1.05$).

6. Closing Remarks on the Successful Year 1 Program

The above project was conceived as a two-year program in terms of developing of *true coilable* crystalline fibers themselves. In Year 1, we pursued the development of fully crystalline fiber structures (double-clad structures with doped crystalline core and undoped crystalline cladding), without pursuing the “coilability” aspect of it. The major purpose of the Year 1 program was to develop baseline knowledge of fiber fabrication accuracy and fiber quality (core and clad propagation loss), and figure out how to best take advantage of clad pumping and what the expected maximum efficiency of the fiber structures that can be made using the AFB fabrication technology is. We have succeeded in all of our Year 1 goals. We fabricated several high quality testable fiber structures and demonstrated world-class laser results with them—which is pretty outstanding for the Year 1 project.

Here, in brief, are the world's firsts and world-record results:

- We developed and tested a highly efficient, resonantly diode-pumped Er:YAG-core, double-clad, all-crystalline eye-safe waveguide laser. An $\text{Er}^{3+}(1\%)\text{:YAG}$ single-crystalline core with an ultra low NA of ~0.02 was embedded in an undoped single-crystalline YAG cladding and over-clad by transparent MgAl_2O_4 ceramic. The waveguide was CW clad-pumped by a spectrally-narrowed, indium gallium arsenide phosphide (InGaAsP)/indium

phosphide (InP) laser diode module at \sim 1532 nm. We achieved 25.4 W of output power at 1645 nm with a beam quality of $M^2 \sim 2.6$. The achieved 56.6% slope efficiency with respect to the absorbed pump was limited by scattering loss of the pump light in the inner cladding (YAG-spinel interface). To the best of our knowledge, this is the first reported laser experiment with crystalline RE-doped YAG-core and a truly double-clad crystalline square waveguide structure.

- We developed and demonstrated CW operation of a resonantly pumped Er:YAG single-mode channel waveguide laser with diffraction-limited output and nearly quantum defect limited efficiency. Using a longitudinally core-pumped, nearly square (61.2 μm x 61.6 μm) Er^{3+} :YAG-core waveguide embedded in an undoped YAG cladding, an output power of 9.1 W with the slope efficiency of 92.8% (vs. absorbed pump power) has been obtained. To the best of our knowledge, this optical-to-optical efficiency is the highest ever demonstrated for any channel waveguide laser at room temperature. All of that was achieved with a nearly Gaussian output beam, $M^2 = 1.05$, and 1000:1 degree of output polarization.

Unfortunately the project has not been selected for Year 2 funding—so all of the planned final fiber structures, including true coilable, full-length, fully crystalline fibers have never been fabricated. Accordingly, the highly scalable laser demonstrations with full-planned-length coilable structures never happened.

Based on the results of Year 1 and discussions that led to plans for Year 2, some comments can be made regarding the likelihood of scaling this approach to “high energy laser” levels, that is, to powers on the order of 100 kW, or at least a few tens of kW. Raytheon’s Robust Electric Laser Initiative (RELI) program results suggest that planar waveguide gain elements of lengths around 300 mm can produce powers in the 20–30 kW range. The goal of Year 2 of the coilable crystalline fiber project was to reach lengths of 100–200 mm. Since Year 1 results showed that it is difficult to obtain spinel of that length with sufficiently high quality, Onyx and ARL planned in Year 2 to switch the outer cladding to sapphire. Subsequent work is making it significantly more plausible that double-clad waveguides 200 mm long can be made using sapphire cladding and Onyx bonding technology. It is more difficult to predict how much farther than that the technology can be extended. This suggests that this bonding approach to all-crystalline, double-clad coilable waveguides may reach relevant power levels, at least if a few stages of amplification or the combining of a few beams can be employed.

However, we see the main goal of this project as having been investigation of the feasibility of double-clad crystalline waveguides with fiber-like dimensions (in particular, thin enough to be coilable,) using available technology (bonding). That is, they provide an early test of the potential of all-crystalline fibers without waiting for further progress on the fabrication of such fibers, even if true fiber fabrication without bonding remains the more promising long-term scaling approach. We believe that the good laser results reported in the appendices do indeed demonstrate that potential.

7. References

1. Brown, D. C.; Hoffman, H. J. Thermal, Stress, and Thermo-Optic Effects in High Average Power, Double-Clad Silica Fiber Laser. *IEEE J. of Quantum Electron.* **2001**, *37*, 207.
2. Stacey, C. D.; Jenkins, R. M.; Banerji, J.; Davies, A. R. Demonstration of Fundamental Mode Only Propagation in Highly Multimode Fiber for High Power EDSAs. *Opt. Comm.* **2007**, *269*, 310.
3. Dawson, J. W.; Messerly, M. J.; Heebner, J. E.; Pax, P. H.; Sridharan, A. K.; Bullington, A. L.; Beach, R. J.; Siders, C. W.; Barty, C.P.J.; Dubinskii, M. Power Scaling Analysis of Fiber Lasers and Amplifiers Based on Non-Silica Materials. *Proc. SPIE* **2010**, *7686*, 768611-1–768611-12.
4. Parthasarathy, T. A.; Hay, R. S.; Fair, G.; Hopkins, F. K. Predicted Performance Limits of Yttrium Aluminum Garnet Fiber Lasers. *Optical Engineering* **2010**, *49*, 094302-1–094302-8.
5. Ter-Gabrielyan, N.; Fromzel, V.; Mu, X.; Meissner, H.; Dubinskii, M. High Efficiency, Resonantly Diode Pumped, Double-Clad, Er:YAG-Core, Waveguide Laser. *Opt. Express* **2012**, *20*, 25554–25561.
6. Griebner, U.; Schonnagel, H. Laser Operation With Nearly Diffraction-Limited Output From a Yb:YAG Multimode Channel Waveguide. *Optics Letters* **1999**, *24*, 750–752.
7. Mu., X.; Meissner, H.; Lee, H.-C.; Dubinskii, M. True Crystalline Fibers: Double-Clad Design Concept of Tm:YAG-Core Fiber and Mode Simulation. *Proc. SPIE* **2012**, *8237*, 82373M.
8. Beach, R. J.; Mitchell, S. C.; Meissner, H. E.; Meissner, O. R.; Krupke, W. F.; McMahon, J. M.; Bennett, W. J.; Shepherd, D. P. Continuous Wave and Passive Q-Switched Cladding-Pumped Planar Waveguide Lasers. *Opt. Lett.* **2001**, *26*, 881–883.
9. Lee, H. C.; Mu, X.; Meissner, H. E. Interferometric Measurements of Refractive Index Difference Applied to Composite Waveguide Lasers. *Proc. CLEO, AMB4*, 2011.
10. Refractive Index Database.
<http://refractiveindex.info/?group=CRYSTAL&material=Y3Al5O12> (accessed Nov 2012).
11. Vainshtein, L. A. *Open Cavities and Open Waveguides*; Golem Press, 1969.
12. Chiang, K. S. Analysis of Optical Fibers by the Effective-Index Method. *Appl. Opt.* **1986**, *25*, 2169.

13. Setzler, S. D.; Francis, M. P.; Young, Y. E.; Konves, J. R.; Chicklis, E. P. Resonantly Pumped Eyesafe Erbium Lasers. *IEEE J. of Sel. Topics in Quantum Electron.* **2005**, *11*, 645–657.

INTENTIONALLY LEFT BLANK.

Appendix A. High Efficiency, Resonantly Diode Pumped, True Double-Clad, Er:YAG-Core, Waveguide Laser

Ter-Gabrielyan, N.; Fromzel, V.; Mu, X.; Meissner, H.; Dubinskii, M. *Optics Express* **2012**, *20* (23), 25554–25561.

Solid state lasers with a waveguiding gain element have been introduced soon after the first laser was launched (1). In his very original implementation E. Snitzer utilized a round cross-section solid clad/core glass structure (double-clad fiber, with the second cladding simply being the ambient air). Originally, this structure was aimed predominantly at achieving good beam quality based on a low numerical aperture (NA) of the core. This round step-index waveguiding architecture has become the mainstream design of all glass based fiber lasers and amplifiers (e.g., [2]). In their “true double-clad” implementation (the second cladding is a low-index polymer coating) the large cladding NA and relatively large cladding diameter (versus core) greatly facilitate pump power scaling and pump confinement within the fiber, while the small waveguiding core diameter and its small NA serve the purpose of forming a nearly diffraction-limited output beam.

The idea of substituting low thermal conductivity glass in fibers with a high thermal conductivity single crystal for further power scaling has led to fiber architectures in the form of relatively thin and long crystalline rods manufactured by either laser heated pedestal growth (LHPG) (3) or micro-pulling-down (4) techniques. These air-clad rod-like fibers have a very high NA, so they are utilized to facilitate the collection and confinement of a laser diode pump emission along the entire rod-fiber length (4, 5). But in this case, the laser’s good beam quality cannot be achieved without a proper external cavity, which compromises the original idea of forming an output beam with waveguiding alone. In addition, a spatial matching of pump and laser modes, formed by the cavity design, is never complete. For that reason the rod-like fibers will always have to remain short - thus, forfeiting the benefits of the fiber’s large surface area to volume ratio-for efficient thermal management.

Recently, successful efforts in true double-clad (DC) crystalline core fibers were reported, where the DC structure was fabricated using the co-drawing laser-heated pedestal growth (CDLHPG) technique (e.g., [6, 7]). The first cladding was made of glass, which can provide a good laser beam quality through core waveguiding. However, glass introduces a much higher thermal resistance between the crystalline core and the heat sink - a major hindrance for power scaling.

To this day, the idea of fully crystalline double-clad waveguiding devices for bulk solid-state lasers has only been proven feasible when researchers turned away from conventional round cross-section clad/core structures to rectangular shapes – a planar waveguide or a channel waveguide. Among the best achievements was a Yb:YAG or Nd:YAG planar waveguide,

directly cladding-pumped by two laser diode bars (8). This laser demonstrated optical-to-optical slope efficiency of 50% and was single-mode in the guided direction ($\sim 8 \mu\text{m}$) and highly multimode in the unguided direction” ($\sim 500 \mu\text{m}$). In another demonstration, a Yb:YAG channel waveguide with the nearly square core-clad structure was directly pumped into the core by a single laser diode bar (9). It yielded a nearly diffraction-limited output in both directions and an optical-to-optical slope efficiency of 43% (9). In both (8) and (9) experiments, transverse pumping was used. The end pumping of the planar waveguiding structure was successfully implemented in (10). In the (8, 10) the gain elements were fabricated using adhesion-free bonding (AFB)¹ of the thin, Nd- or Yb-doped YAG cores and the undoped YAG cladding to form a planar, waveguiding structure. Based on some experimental demonstrations pursuing significant power scaling (e.g., [8–11]), adhesion-free bonding is a promising technique for fabrication of true double-clad and even triple-clad, fully crystalline, bulk structures. Available data on utilizing AFB-fabricated double-clad waveguides for power scaling is still scarce, requiring further investigation of these structures for better understanding of their potential.

Here we report our first laser results obtained with a fully crystalline, double-clad, channel-waveguide structure, fabricated by AFB, which we consider to be the first iteration on the path toward a highly scalable, single-mode, waveguide laser. We demonstrated a resonantly cladding-pumped, waveguide laser with an Er^{3+} :YAG core. It operated at 1645 nm with a slope efficiency of over 56% when directly pumped at $\sim 1532 \text{ nm}$ by a low-brightness, fiber coupled, InGaAsP/InP laser diode module. To the best of our knowledge, this is the first reported experiment with a Er^{3+} -doped, true double-clad, crystalline, channel waveguide structure.

Experimental Setup

The investigated 30 mm long, double-clad waveguiding gain element was fabricated using the AFB process. The waveguide has a square active core made of a single-crystalline Er^{3+} (1%):YAG with a $500 \times 500 \mu\text{m}$ cross-section, see figure A-1. The core was clad by an undoped YAG forming the first cladding with a $700 \times 700 \mu\text{m}$ cross-section. The refractive index of the core is higher than the refractive index of an undoped YAG in the first cladding by $\sim 1.04 \times 10^{-4}$. This difference provides the required waveguiding. Taking the refractive index of Er:YAG at 1532 nm as 1.8073 (12), the core has an ultra-low NA of ~ 0.02 . The outer cladding with the $1 \times 8 \text{ mm}$ cross-section was fabricated from transparent spinel ceramic (MgAl_2O_4) with a refractive index of 1.695 at 1532 nm . Thus, the NA of the first cladding for the pump emission (1532 nm) was ~ 0.627 . The large NA allowed us to use pump beams with an angular divergence up to $\sim 78^\circ$ for pump delivery into the cladding. The rendering of the entire double-clad structure with its dimensions is depicted in figure A-1b. Both ends of the Er:YAG waveguide were anti-reflection (AR) coated for the spectral range of 1500 – 1680 nm . The waveguide was clamped

¹Depending on the source, diffusion bonding (9) process is also referred to in literature as “thermal bonding” (8) or “direct bonding” (10), but recently the terminology is most often converging to a term “adhesion-free bonding” (AFB) (11, 14).

between the water-cooled, copper plates and conductively cooled from the top and the bottom. The temperature of the cooling water was maintained at 18 °C.

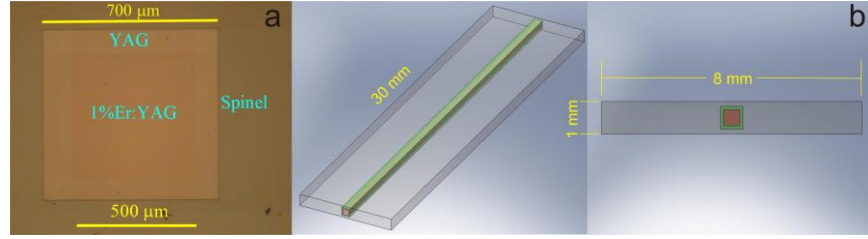


Figure A-1. (a) The end-face photograph of the double-clad, Er^{3+} :YAG-core, channel waveguide, as described in the paper body; core – single-crystalline Er^{3+} (1%):YAG, inner cladding – single-crystalline undoped YAG, outer cladding - transparent ceramic magnesium aluminum spinel (MgAl_2O_4) and (b) The rendering of the waveguide with overall dimensions.

A simplified optical layout of our experimental set-up is shown in figure A-2. The pump source was a spectrally narrowed (~2 nm full width half maximum, FWHM), fiber coupled, water cooled, InGaAsP/InP laser diode module (FCLDM). The fiber core had a 1 mm diameter and a 0.22 NA. The wavelength of this diode laser could be temperature-tuned by varying the coolant temperature of the stack. A combination of a polarizer and a half-wave plate inside the laser diode module was used as a variable pump power attenuator.

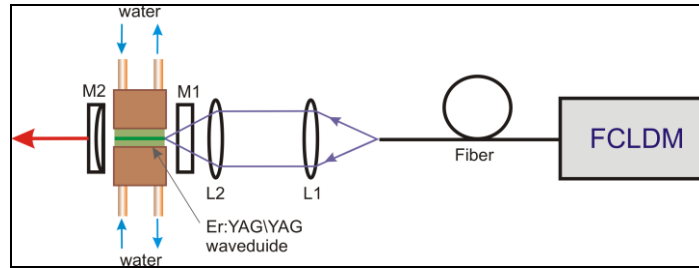


Figure A-2. A simplified optical layout of the cladding-pumped Er:YAG/YAG channel waveguide laser. The pumping source, a fiber coupled InGaAsP/InP laser diode module (FCLDM) at 1532 nm, is described in the paper body. M1 and M2 are the cavity mirrors. L1 and L2 are the lenses of pump coupling optics.

The pump radiation was collimated by a lens $L1$ with a focal length of $F_1 = 40 \text{ mm}$. The collimated pump beam was focused through a flat dichroic mirror $M1$ ($T > 98\%$ at 1520–1540 nm, $R > 99.55\%$ at 1590–1650 nm) into the inner cladding of the Er:YAG waveguide by an aspheric lens $L2$. Three different aspheric lenses with focal lengths of $F_2 = 30 \text{ mm}$, 25.4 mm , and 20 mm were used in the $L2$ position, which resulted in a pump $NA = 0.425$, 0.5 , and 0.635 , respectively. The best performance was obtained with a $F_2 = 20 \text{ mm}$. In this case, the pump beam diameter on the waveguide face was $\sim 650 \mu\text{m}$ (at e^{-2} level). The laser cavity was formed by a flat dichroic mirror, $M1$, and a concave output coupler (OC), $M2$. Radii of curvature (RoC) of the OC varied between 50 and 100 mm and their reflectivities varied between 85% and 68%. The

cavity length was set to *35 mm* for the OC with a RoC of *50 mm* and to *110 mm* for the OC with the RoC of *100 mm*.

An absorption spectrum of Er:YAG at room temperature (see figure A-3), associated with resonant $^4I_{15/2} \rightarrow ^4I_{13/2}$ transitions of the Er^{3+} ion, has several maxima between *1524 nm* and *1540 nm* which can be used for pumping. The pumping wavelength of the FCLDM was adjusted to the vicinity of the strongest *1532 nm* absorption peak, see figure A-3. The pump wavelength was monitored by an optical spectrum analyzer (Yokogawa, model AQ6370C) with the spectral resolution set to *0.1 nm*.

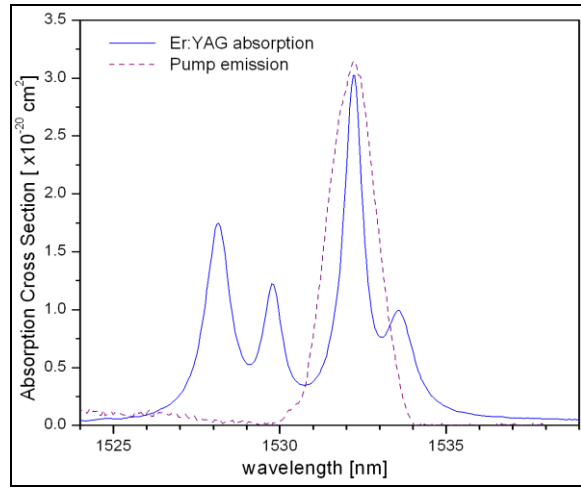


Figure A-3. The absorption cross-section of the $^4I_{15/2} \rightarrow ^4I_{13/2}$ transitions of Er^{3+} in YAG at *300 K* (blue, solid line). Spectrum of the laser diode module (purple, dashed line).

Experimental Results: Er:YAG Double-Clad Waveguide Laser with Nonselective Cavity

The optimized CW performance of the resonantly pumped, double-clad Er:YAG waveguide laser is presented in figure A-4. The *35 mm* long, plano-concave laser cavity used an OC with the RoC of *50 mm* and $\sim 85\%$ reflectivity. The best optical-to-optical slope efficiency with respect to the incident pump power was *31.4%*. This efficiency was lower than we expected based on our preliminary modeling, therefore, we carefully analyzed the power balance of this laser. Despite the considerable reduction in the effective pump absorption of the double-clad, Er:YAG-core waveguide (per clad-to-core ratio), the pump saturation effects, nevertheless, can be important for resonantly pumped Er:YAG (13). The absorption of the Er-doped crystals is usually saturated in the gain medium without lasing and experiences partial or full “recovery” to its unsaturated level with growing intensity of the laser emission in the cavity. To evaluate the absorbed pump power correctly, we measured the incident and the transmitted pump power as well as the laser output power simultaneously. It should be noted, that in the case of the cladding-pumped waveguide laser, the calculated absorbed pump power, determined as the difference between the incident and the transmitted pump power, can be severely affected by the scattering losses in the

inner cladding. In order to estimate the possible contribution of this effect we separately measured the passive transmission of the waveguide. A widely tunable, narrow-bandwidth (1 MHz) semiconductor laser source (Santec, model TLS-210) was tuned to the 1524 nm (or 1540 nm) wavelength, where there is practically no Er^{3+} absorption (see figure A-3). Its output beam was shaped to reproduce the NA and dimensions of the actual pump beam at the entrance face of the waveguide. We also assumed that passive losses in the Er:YAG core at pumping (1532 nm) and lasing (1645 nm) wavelengths are the same.

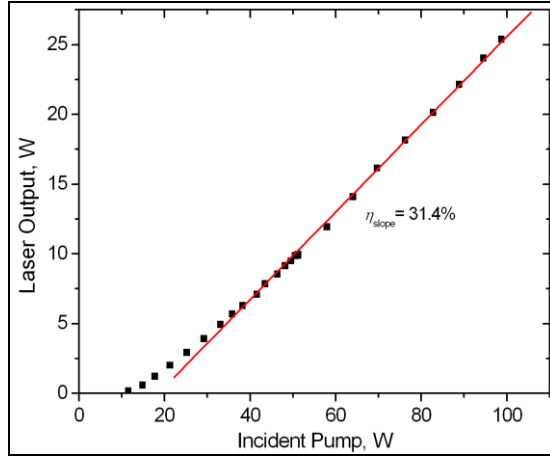


Figure A-4. The output power of the Er(1%):YAG/YAG channel waveguide laser at 1645 nm versus the incident pump power. Laser cavity: $L_{cav} = 35\text{ mm}$, flat HR mirror, output coupler with the reflectivity of $R_{OC} = 85\%$, $RoC = 50\text{ mm}$.

The passive transmission of the waveguide measured in this manner was found to be $T = 78\%$. After taking into account the residual reflection of the AR coatings at these wavelengths ($\sim 1.0\%$ on each waveguide end, according to the vendor's specification), we arrived at the passive loss figure of $\alpha = 0.07\text{ cm}^{-1}$ (which translates to a $\sim 30\text{ dB/m}$). This steep loss figure can explain the relatively low waveguide laser efficiency versus the incident pump power. In this situation the laser output versus the absorbed pump power is a better representation of laser efficiency and scaling potential.

Figure A-5 indicates the Er:YAG channel waveguide laser output power at 1645 nm versus the absorbed pump power at 1532 nm , calculated using the procedure described above and taking into account the measured pump scattering loss. The best slope efficiency of 56.6% versus the absorbed pump power was achieved with a 85% reflectivity of the OC. A lower slope efficiency of 50.3% was achieved with 72% OC reflectivity. The maximum achieved CW output power at 1645 nm was 25.4 W. The measured fraction of the absorbed pump power during lasing varied from $\sim 63\%$ to $\sim 52\%$ depending on the pump power density. As seen in figure A-5, the dependence is perfectly linear, so power scaling of the laser at this point is strictly pump limited.

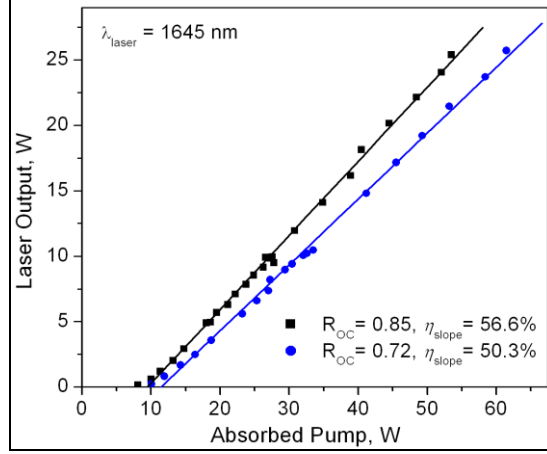


Figure A-5. Laser output power at 1645 nm of the resonantly diode cladding-pumped at 1532 nm Er(1%):YAG-core, channel waveguide laser versus the absorbed pump power. Maximum slope efficiency of $\sim 56.6\%$ was achieved with the output coupler reflectivity of 85%.

With the expected multimode nature of the Er:YAG core in mind², we measured the output beam divergence with a 1.6- μm -sensitive IR camera (Spiricon, model LW230). The camera was placed in the focal plane of the concave reflector with a 500 mm radius of curvature ($f = 250\text{ mm}$). We found that at the maximum output power of the waveguide laser, the beam divergence was $\sim 13.4\text{ mrad}$ in both directions. The cavity length was $L = 35\text{ mm}$ and the output corresponded to the multimode regime with $M^2 \sim 2.6$. This beam quality is comparable to that achieved in the guided direction with a $35\text{ }\mu\text{m}$ -core, single-mode planar waveguide (14). Compared to a rod-like fiber laser (15), which demonstrated beam quality of $M^2 \sim 15$, our laser has $\times 2.5$ higher brightness, despite having 10-times lower output power.

With a longer laser cavity of 110 mm and the output coupler with the RoC of 100 mm , by slightly misaligning the OC, it was possible to achieve nearly TEM_{00} operation, but at a considerably lower ($\times 3$ - 4 times) output power. A measured angular divergence was $\sim 6\text{ mrad}$. Typical intensity distributions in the focal plane of the reflector (far field) for the highly multimode (left) and nearly- TEM_{00} -mode beams is shown in figure A-6.

²A calculated B-number is ~ 13 (a *B-number* is a square-core, channel waveguide analog of a *V-number* of conventional round-core fibers [16]).

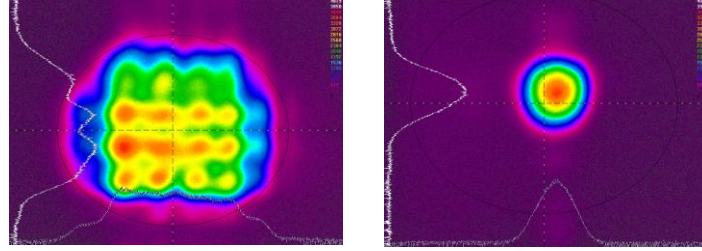


Figure A-6. Far field intensity distribution of the double-clad, channel waveguide Er:YAG laser. Left: 35 mm-long plano-concave laser cavity, $RoC = 50 \text{ mm}$, $R_{OC} = 85 \%$, $P_{PUMP} = 98 \text{ W}$, $P_{OUT} = 25.4 \text{ W}$, divergence $\sim 13.4 \text{ mrad}$. Right: slightly misaligned, 110 mm-long, plano-concave laser cavity, $RoC = 100 \text{ mm}$, $R_{OC} = 70 \%$; $P_{PUMP} = 70 \text{ W}$, $P_{OUT} = 8 \text{ W}$, divergence $\sim 6 \text{ mrad}$.

Experimental Results: Er:YAG Double-Clad Waveguide Laser with Selective Cavity

The pump power density, which was achieved in the active Er:YAG core by cladding-pumping with a FCLDM, is very high, in excess of 20 kW/cm^2 . In fact, it is higher than the pump power density reported in most of the end-pumped Er:YAG lasers, even those pumped by Er-fiber lasers (e.g., [17]). This feature is very important for Er:YAG lasers designed to exploit the 1617-nm laser transition of Er^{3+} , for the following reasons. Both 1645-nm and 1617-nm laser lines correspond to different inter-Stark transitions between the energy levels of $^4I_{13/2}$ and $^4I_{15/2}$ manifolds of Er^{3+} in YAG. The terminal level of the 1617 nm laser transition is much closer to the ground state, and its Boltzmann population at room temperature is ~ 0.036 , versus ~ 0.021 for the 1645 nm one. As a result, the 1617 nm lasing has higher ground-state absorption (GSA) loss. This difference in GSA loss is not fully compensated by the higher emission cross-section of the 1617 nm transition, especially at low pump densities. Therefore, in order to “force” the Er:YAG waveguide laser to operate at 1617 nm , it is necessary to use a wavelength-selective cavity or to achieve relatively larger inversion density which will help to suppress the 1645 nm lasing (17, 18). In our experiment we used the 35 mm long cavity formed by a flat nonselective HR mirror, and a concave, wavelength-selective output coupler ($R_{OC} = 62 \%$ at 1617 nm , $R_{OC} = 21 \%$ at 1645 nm) with the RoC of 50 cm. With this cavity, the laser operates only at $\sim 1617 \text{ nm}$ (the peak of laser emission was measured at 1616.6 nm , $\Delta\lambda \sim 0.6 \text{ nm}$ at e^{-2} level). Figure 7 shows the output power of the Er:YAG waveguide laser operating at 1616 nm versus the incident pump power.

As can be seen from figure A-7, the laser output grew linearly with the pump power, reaching the maximum of 8.05 W (slope efficiency $\sim 13\%$). Due to a limited choice of available concave output couplers with the required wavelength selectivity, this laser has not been optimized. The accurate measurements of the absorbed pump power in these experiments were also not feasible because the wavelength-selective OC had a very low transmission at the pump wavelength ($T < 0.01\%$), and the transmitted pump power could not be determined correctly.

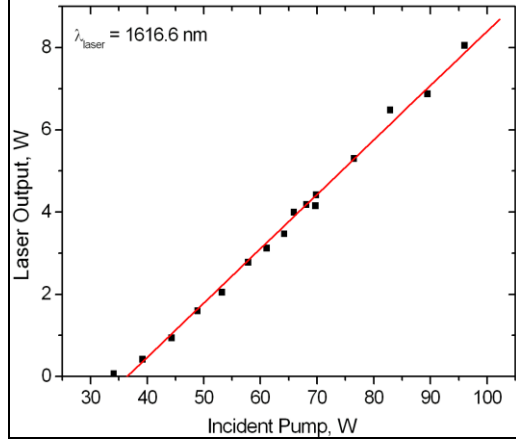


Figure A-7. The output power of the Er:YAG channel waveguide laser operated at 1617 nm versus the incident pump power. Wavelength selective laser resonator: $L_{CAV} = 35\text{ mm}$, $R_{OC} = 62\%$ at 1617 nm , $R_{OC} = 21\%$ at 1645 nm .

Conclusions

In conclusion, we demonstrated, what is believed to be, the first resonantly diode-pumped, Er:YAG-core, double-clad, channel waveguide laser. The waveguide was designed with the single-crystalline $\text{Er}^{3+}(1\%)\text{:YAG}$ core, undoped single-crystalline YAG cladding and overclad with transparent magnesium aluminum spinel (MgAl_2O_4) ceramic. The resonant clad-pumping was performed by a spectrally narrowed ($\sim 2\text{ nm FWHM}$), fiber coupled InGaAsP/InP laser diode module at $\sim 1532\text{ nm}$. The highly efficient waveguide laser delivered a pump power limited $\sim 25.4\text{ W}$ of the multimode CW output power at 1645 nm . Despite the multimode gain element core used in this first experiment, the measured beam quality of $M^2 \geq 2.6$ was achieved with the optical-to-optical slope efficiency of 56.6%. The same waveguide laser, but with an un-optimized wavelength-selective cavity, delivered $\sim 8\text{ W}$ of CW output power at 1616.6 nm . These results, obtained with the fully crystalline, truly double-clad, channel waveguide, are our first iteration on the path toward highly power scalable, nearly diffraction-limited output laser.

References

1. Snitzer, E. Optical Maser Action of Nd³⁺ in A Barium Crown Glass. *Phys. Rev. Lett.* **1961**, *7*, 444–446.
2. Mackenzie, J. I. Dielectric Solid-State Planar Waveguide Lasers: A Review. *IEEE JSTQE* **2007**, *13*, 626–637.
3. Feigelson, R. S.; Kway, W. L.; Route, R. K. Single-Crystal Fibers by the Laser-Heated Pedestal Growth Method. *Optical Engineering* **1985**, *24*, 1102–1107.
4. Sangla, D.; Martial, I.; Aubry, N.; Didierjean, J.; Perrodin, D.; Balembois, F.; Lebbou, K.; Brenier, A.; Georges, P.; Tillement, O.; Fourmigué, J.-M. High Power Laser Operation With Crystal Fibers. *Appl. Phys.* **2009**, *B97*, 263–273.
5. Bibeau, C.; Beach, R. J.; Mitchell, S. C.; Emanuel, M. A.; Skidmore, J.; Ebbers, C. A.; Sutton, S. B.; Jancaitis, K. S. High-Average-Power 1-μm Performance and Frequency Conversion of a Diode-End-Pumped Yb:YAG Laser. *IEEE J. Quant. Electron.* **1998**, *34*, 2010–2019.
6. Lo, C.-Y.; Huang, K.-Y.; Chen, J.-C.; Tu, S.-Y.; Huang, S.-L. Glass-clad Cr⁴⁺:YAG Crystal Fiber for the Generation of Superwideband Amplified Spontaneous Emission. *Opt. Lett.* **2004**, *29*, 439–441.
7. Lai, C.-C.; Ke, C.-P.; Liu, S.-K.; Jheng, D.-Y.; Wang, D.-J.; Chen, M.-Y.; Li, Y.-S.; Yeh, P. S.; Huang, S.-L. Efficient and Low-Threshold Cr4+:YAG Double-Clad Crystal Fiber Laser. *Opt. Lett.* **2011**, *36*, 784–786.
8. Beach, R. J.; Mitchell, S. C.; Meissner, H. E.; Meissner, O. R.; Krupke, W. F.; McMahon, J. M.; Bennett, W. J. Continues-Wave and Passive Q-Switched Cladding-Pumped Planar Waveguide Lasers. *Opt. Lett.* **2001**, *26*, 881–883.
9. Griebner, U.; Schonnagel, H. Laser Operation with Nearly Diffraction-Limited Output From a Yb:YAG Multimode Channel Waveguide. *Opt. Lett.* **1999**, *24*, 750–752.
10. Mackenzie, J. I.; Shepherd, D. P. End-Pumped, Passively Q-switched Yb:YAG Double-Clad Waveguide Laser. *Opt. Lett.* **2002**, *27*, 2161–2163.
11. Mu, X.; Meissner, H.; Lee, H.-C.; Dubinskii, M. True Crystalline Fibers: Double-Clad LMA Design Concept of Tm:YAG-Core Fiber and Mode Simulation. *Proc. of SPIE* **2012**, 8237, 82373M-1–82373M-2.
12. <http://refractiveindex.info/?group=CRYSTAL&material=Y3Al5O12>
13. Sato, Y.; Taira, T. Saturation Factors of Pump Absorption in Solid-State Lasers. *IEEE J. of Quantum Electron.* **2004**, *40*, 270–280.

14. Mackenzie, J. An Efficient High-Power 946 nm Nd:YAG Planar Waveguide Laser. *Appl. Phys.* **2009**, *B97*, 297–306.
15. Belen, X.; Piehler, S.; Didierjean, J.; Aubry, N.; Voss, A.; Graf, T.; Balembois, F.; George, P. 250 W Single-Crystal Fiber Yb:YAG Laser. *Opt.Lett.* **2012**, *37*, 2898–2900.
16. Chiang, K. S. Dual Effective-Index Method for the Analysis of Rectangular Dielectric Waveguides. *Appl. Opt.* **1986**, *25*, 2169–2174.
17. Setzler, S. D.; Fransis, M. P.; Young, Y. E.; Konves, J. R.; Chicklis, E. P. Resonantly Pumped Eyesafe Erbium. *IEEE J. of Select. Topics in Quantum Elect.* **2005**, *11*, 645–657.
18. Spariosu, K.; Leyva, V.; Reeder, R. A.; Klotz, M. J. Efficient Er:YAG Laser Operating at 1645 and 1617 nm. *IEEE J. Quant. Electron.* **2006**, *42*, 182–186.

Appendix B. Resonantly-Pumped Single-Mode Channel Waveguide Er:YAG Laser With Nearly Quantum Defect Limited Efficiency

Ter-Gabrielyan, N.; Fromzel, V.; Mu, X.; Meissner, H.; Dubinskii, M. *Optics Letters* **2013**, *38* (14), 2431–2433.

Fully crystalline channel waveguide lasers are very promising as efficient and compact sources for many laser applications requiring significant power scaling with nearly diffraction-limited beam quality. In a double-clad implementation they are direct analogs of conventional (glass-based) fiber lasers with the same ability to maintain high clad-pump intensity and tight confinement of both pump and laser modes along the entire length of the gain medium. Analysis of conventional glass fiber laser power scaling (1, 2) indicates that, due to low glass thermal conductivity, heat generation associated with pumping is still strong. As a result, fibers may reach fracture threshold before nonlinear scaling limits, while nonlinearities, e.g., stimulated Brillouin scattering (SBS), will be a prime power scaling limiter for very narrowband (especially single longitudinal mode, SLM) fiber lasers. As opposed to conventional fibers, fully crystalline double-clad waveguides are more suitable for laser power scaling due to their ~10 times higher thermal conductivity as well as an order of magnitude higher absorption and emission cross sections of common rare-earth (RE) dopants (3). In addition, Yttrium Aluminum Garnet (YAG) waveguides have an extremely low SBS gain coefficient from 9×10^{-15} to 5×10^{-12} m/W (variation is based on data from different sources [3]), versus that of silica glass (5×10^{-11} m/W). Estimates indicate that fully crystalline double-clad fiber lasers can be scaled to tens of kilowatts of power even in the most demanding SLM laser design (3, 4). Therefore, small-core waveguide laser development is of great importance.

Recently, a resonantly cladding-pumped, Er:YAG double-clad waveguide laser, fabricated by an adhesive-free bonding (AFB), has been demonstrated (5). Taking advantage of the large numerical aperture (NA) of the inner cladding, the laser was efficiently pumped by a conventional laser diode bar stack with poor beam quality and delivered 25.4 W of CW output at 1645 nm with 56.6% optical efficiency (limited by high cladding loss). This double-clad crystalline laser had a free-space open cavity, and, due to the large core size ($500 \mu\text{m} \times 500 \mu\text{m}$), it was sufficiently multimode. A nearly diffraction limited output has been demonstrated from a side-pumped multimode small-core ($100 \mu\text{m} \times 80 \mu\text{m}$) Yb:YAG channel waveguide (6). This effort used a free-space open cavity, and despite a very short (10 mm) waveguide length, the achieved slope efficiency was relatively low for resonant pumping (43%) due to imperfect matching of the pump and laser modes.

In this work, we demonstrate a small-core, resonantly-pumped, single-mode, Er:YAG channel waveguide laser with diffraction limited output and nearly quantum defect limited efficiency. This first core-pumped {Er³⁺:YAG-core/undoped YAG cladding} waveguide laser delivered a

9.1 W CW output with slope efficiency of 92.8% (versus the absorbed pump power) and $M^2 = 1.05$.

Experimental Setup

The investigated 41.3 mm long channel waveguide, manufactured by AFB (6–8), had a $61.2 \mu\text{m} \times 61.6 \mu\text{m}$ cross-section $\text{Er}^{3+}(0.25 \text{ at.\%}):YAG$ core. An active channel was embedded in a $3 \text{ mm} \times 5 \text{ mm}$ YAG cladding. For ease of fabrication the channel was buried in the cladding only $30 \mu\text{m}$ deep under the $5 \text{ mm} \times 41.3 \text{ mm}$ surface. The small refractive index difference, Δn , between the Er-doped YAG core and undoped YAG cladding provides sufficient waveguiding with low NA (8). This Δn was measured (with the accuracy of $\sim 10^{-6}$) by the interferometric method with specially prepared adhesive-free bonded {Er:YAG/YAG} test samples for several Er^{3+} concentration values (9). Given the refractive index of the undoped YAG cladding at 1532 nm of 1.8073 (10) and the measured $\Delta n = 5.2 \times 10^{-5}$ between the $\text{Er}^{3+}(0.25 \text{ at.\%}):YAG$ and undoped YAG, the core NA was derived to be ~ 0.014 . Such an ultra-low NA of the core should lead to a single transverse mode operation of the channel waveguide despite its relatively large (on the scale of step-index conventional fibers) core cross-section. However, the ultra-low NA presents a challenge for achieving efficient pump launching into the core from sources with large angular divergence. To get around this problem, a single transverse mode Er-fiber laser was used as a pump source in this case. Both ends of the Er:YAG waveguide were anti-reflection (AR) coated for both laser and pump wavelengths ($R = 0.25\%$ for 1525 – 1650 nm). The waveguide was mounted on a water-cooled platform and conductively cooled at 18°C .

The experimental layout of the channel waveguide laser is shown in figure B-1a. The CW Er-fiber laser ($\sim 0.3 \text{ nm}$ full-width at half-maximum at $\sim 1532 \text{ nm}$), longitudinally pumped the Er:YAG-core. A collimated fiber laser output with a divergence of $\sim 1 \text{ mrad}$ was focused into the waveguide core by an aspheric lens L_1 through a plano-plano dichroic mirror (HR for 1600–1650 nm, AR for the pump). The laser cavity was formed by the above mentioned dichroic mirror and a plano-concave output coupler (OC). Both mirrors were placed at less than $40 \mu\text{m}$ from the waveguide ends. An analysis of open-cavity modes shows that the excitation of the TEM_{00} laser mode in such a cavity is impossible due to the high diffraction loss and only a waveguiding mode can be supported (11).

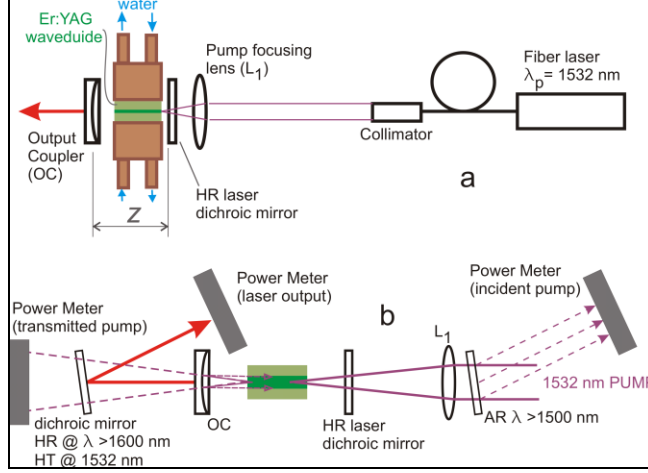


Figure B-1. (Color online) (a) Experimental layout of the Er:YAG-core channel waveguide laser pumped by a single-mode Er-fiber laser. (b) Optical layout used for simultaneous measurements of the incident and transmitted pump power along with the laser output power.

Several OCs with radii of curvature (RoC) between 100 and 2000 mm and reflectivities (R_{OC}) between 70% and 90% at laser wavelengths were used for laser optimization.

An optical spectrum analyzer (Yokogawa, model AQ6370C) with the spectral resolution set to 0.1 nm was used for measuring spectral outputs of the pump and channel waveguide lasers.

The laser beam divergence was determined with an IR CCD camera (Spiricon, model LW230) placed in the focal plane of the spherical lens with a focal length of $f = 150 \text{ mm}$.

Due to the short length of the waveguide, not all of the incident power is absorbed on the first pass. In order to derive the maximum achievable optical-to-optical efficiency of the waveguide laser, one has to measure the un-absorbed pump power reflected off the OC back into the waveguide. Figure B-1b depicts the optical layout used for simultaneous measurements of the incident and transmitted pump power along with the laser output power, from all of which the absorbed pump power is derived. The accuracy of the entire derivation also relies on precise knowledge of transmissions and reflections of all optical components used in the setup shown in figure B-1b. More detailed analysis of this technique including both single-pass and double-pass core absorption cases will be discussed elsewhere.

Experimental Results

Figure B-2a shows the CW output power of the Er:YAG-waveguide laser versus the incident pump power at 1532 nm. The maximum output power of 9.1 W and the best optical-to-optical efficiency of 49.2% were achieved with the $R_{OC} = 80\%$, $RoC = 50 \text{ mm}$ and the pump focusing lens L_1 with $f_1 = 50 \text{ mm}$. This lens provides the best match between the converging pump beam and the channel waveguide NA.

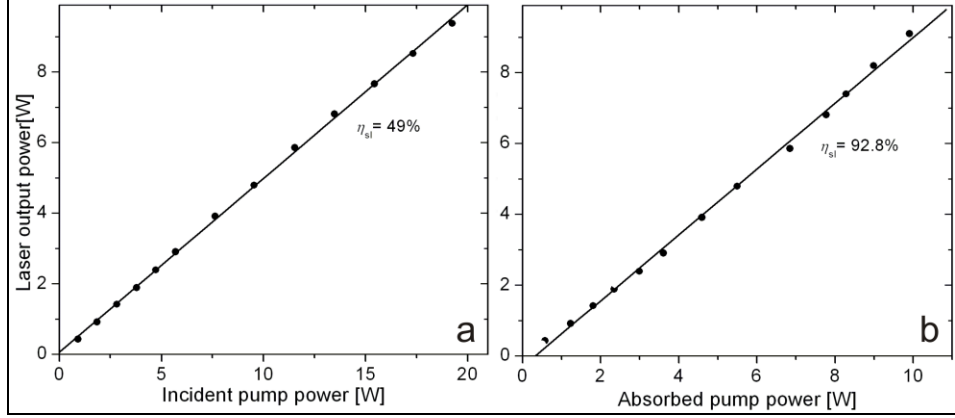


Figure B-2. (a) CW output power of the resonantly pumped Er:YAG-core waveguide laser versus the incident pump power and (b) CW output power versus the absorbed pump power. Laser cavity: length $Z = 41.3$ mm, $R_{OC} = 80\%$, $RoC = 50$ cm. With this R_{OC} the laser exhibited a dual wavelength operation, at 1617 and 1645 nm simultaneously.

In figure B-2b the output power of the waveguide laser is plotted versus the absorbed pump power derived from multi-point power measurements as depicted in figure B-1b. The observed laser slope efficiency is extremely high, and is near the quantum defect limited value for resonant pumping at 1532 nm.

The Er:YAG-core waveguide was designed to be a single-mode device. The criterion of single-mode operation for square waveguides is $B < 1.37$, where B -number, is the “square analog” of the V-number for round fibers (12):

$$B = \frac{2a}{\lambda} NA \quad (B-1)$$

Based on the Er:YAG core NA of 0.014 and the core size of $a = 60$ μm , the B -number of our waveguide is ~ 1.1 , hence, a purely single-mode laser operation should be expected. Laser beam quality of the Er:YAG channel waveguide laser has been assessed at the maximum CW output power of 9.1 W by analyzing the beam intensity distribution in and near the focal plane of the spherical lens with the focal length of $f = 150$ mm. The laser beam had a nearly perfect Gaussian distribution (figure B-3, inset). The measured beam radius (squared) at $1/e^2$ as a function of the imaging plane position is plotted in figure B-3. The beam quality M^2 derived from the above measurements is around 1.05, which proves that our Er:YAG small-core waveguide laser is a purely single-mode device, by design.

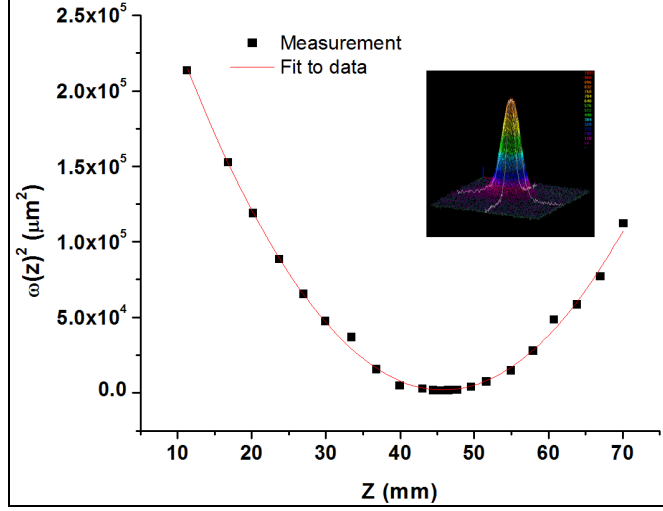


Figure B-3. (Color online) Er:YAG channel waveguide laser beam radius (squared) at $1/e^2$ level as a function of the imaging plane position near the focal plane of the lens $f = 150$ mm. Solid squares – experimental data points, red line – hyperbolic fit to data.

The Er^{3+} :YAG waveguide laser operated simultaneously at two wavelengths, 1617 nm and 1645 nm if the R_{OC} was greater than 75%. It operated at 1617 nm only, if the R_{OC} was below 70%. This observation is in agreement with the well known interplay between the room-temperature emission cross-sections and ground-state absorptions of the 1617-nm and 1645-nm transitions and population inversion of Er^{3+} in YAG (best explained in [13]). The laser output was linearly polarized parallel to the 5-mm side of the cladding facet. The polarization extinction ratio was around 1000:1. This result can be tentatively explained by the asymmetric positioning of the buried waveguiding channel inside the cladding described above. A corresponding asymmetric cooling causes a uniaxial intra-core stress sufficient to polarize the output of the channel waveguide laser.

Conclusions

We demonstrated a CW operation of a resonantly-pumped (at 1532.1 nm) { Er^{3+} :YAG-core/undoped YAG cladding}, single-mode, channel waveguide laser with nearly quantum defect limited efficiency. A core-pumped waveguide delivered a 9.1 W of output power at 1617 and 1645 nm with the slope efficiency of 92.8% (versus the absorbed pump power) and a nearly Gaussian output beam with $M^2 = 1.05$. The demonstrated efficiency is believed to be the highest optical-to-optical efficiency ever demonstrated for a channel waveguide laser at room temperature.

References

1. Brown, D. C.; Hoffman, H. J. Thermal, Stress, and Thermo-Optic Effects in high Average Power, Double-Clad Silica Fiber Laser. *IEEE J. of Quantum Electron.* **2001**, *37*, 207.
2. Stacey, C. D.; Jenkins, R. M.; Banerji, J.; Davies, A. R. Demonstration of Fundamental Mode Only Propagation in Highly Multimode Fiber for High Power EDSAs. *Opt. Comm.* **2007**, *269*, 310.
3. Dawson, J. W.; Messerly, M. J.; Heebner, J. E.; Pax, P. H.; Sridharan, A. K.; Bullington, A. L.; Beach, R. J.; Siders, C. W.; Barty, C.P.J.; Dubinskii, M. Power Scaling Analysis of Fiber Lasers and Amplifiers Based on Non-Silica Materials. *Proc. SPIE* **2010**, *7686*, 768611-1–768611-12.
4. Parthasarathy, T. A.; Hay, R. S.; Fair, G.; Hopkins, F. K. Predicted Performance Limits of Yttrium Aluminum Garnet Fiber Lasers. *Optical Engineering* **2010**, *49*, 094302-1–094302-8.
5. Ter-Gabrielyan, N.; Fromzel, V.; Mu, X.; Meissner, H.; Dubinskii, M. High Efficiency, Resonantly Diode Pumped, Double-Clad, Er:YAG-Core, Waveguide Laser. *Opt. Express* **2012**, *20*, 25554–25561.
6. Griebner, U.; Schonnagel, H. Laser Operation with Nearly Diffraction-Limited Output from a Yb:YAG Multimode Channel Waveguide. *Optics Letters*. **1999**, *24*, 750–752.
7. Mu., X.; Meissner, H.; Lee, H.-C.; Dubinskii, M. True Crystalline Fibers: Double-Clad Design Concept of Tm:YAG-Core Fiber and Mode Simulation. *Proc. SPIE* **8237**, *82373M*, 2012.
8. Beach, R. J.; Mitchell, S. C.; Meissner, H. E.; Meissner, O. R.; Krupke, W. F.; McMahon, J. M.; Bennett, W. J.; Shepherd, D. P. Continues Wave and Passive Q-Switched Cladding-Pumped Planar Waveguide Lasers. *Opt. Lett.* **2001**, *26*, 881–883.
9. Lee, H. C.; Mu, X.; Meissner, H. E. Interferometric Measurements of Refractive Index Difference Applied to Composite Waveguide Lasers. *Proc. CLEO*, AMB4, 2011.
10. <http://refractiveindex.info/?group=CRYSTAL&material=Y3Al5O12>
11. Vainshtein, L. A. *Open Cavities and Open Waveguides*; Golem Press, 1969.
12. Chiang, K. S. Analysis of Optical Fibers by the Effective-Index Method. *Appl. Opt.* **1986**, *25*, 2169.
13. Setzler, S. D.; Fransis, M. P.; Young, Y. E.; Konves, J. R.; Chicklis, E. P. Resonantly Pumped Eyesafe Erbium Lasers. *IEEE J. of Sel. Topics in Quantum Electron.* **2005**, *11*, 645–657.

List of Symbols, Abbreviations, and Acronyms

2-D	two-dimensional
3-D	three-dimensional
AFB	Adhesive-Free Bond
Al_2O_3	aluminum oxide
ARL	U.S. Army Research Laboratory
CCF	coilable crystalline fiber
CTE	coefficient of thermal expansion
CW	continuous wave
DSS	Defense, Security, Sensing
Er	erbium
HEL-JTO	High Energy Lasers Joint Technology Office
InGaAsP	indium gallium arsenide phosphide
InP	indium phosphide
LLNL	Lawrence Livermore National Laboratories
LMA	large mode area
LuAG	lutetium aluminum garnet
MgAl_2O_4	magnesium aluminum spinel
NA	numerical aperture
OPD	optical path difference
RE	rare-earth
RELI	Robust Electric Laser Initiative
SiO_2	silicon dioxide
STM	single-transverse-mode
TEM	transverse electromagnetic

Tm	thulium
YAG or $\text{Y}_5\text{Al}_3\text{O}_{12}$	yttrium aluminum garnet
Yb	ytterbium

1 DEFENSE TECH INFO CTR
(PDF) ATTN DTIC OCA (PDF)

1 GOVT PRINTG OFC
(PDF) A MALHOTRA

2 US ARMY RSRCH LABORATORY
(PDFS) ATTN IMAL HRA MAIL & RECORDS MGMT
ATTN RDRL CIO LL TECHL LIB

3 US ARMY RSRCH LAB
(PDFS) ATTN RDRL SEE M
MARK DUBINSKIY
LARRY D. MERKLE
HELMUTH MEISSNER

INTENTIONALLY LEFT BLANK.